Evidence for Bolgiano-Obukhov scaling in rotating stratified turbulence using high-resolution direct numerical simulations

D. Rosenberg, A. Pouquet, R. Marino, and P. D. Mininni

Citation: Physics of Fluids **27**, 055105 (2015); doi: 10.1063/1.4921076
View online: http://dx.doi.org/10.1063/1.4921076
View Table of Contents: http://scitation.aip.org/content/aip/journal/pof2/27/5?ver=pdfcov
Published by the AIP Publishing

PHYSICS OF FLUIDS **27**, 055105 (2015)

Evidence for Bolgiano-Obukhov scaling in rotating stratified turbulence using high-resolution direct numerical simulations

D. Rosenberg,[1] A. Pouquet,[2] R. Marino,[3,4,5] and P. D. Mininni[6]
[1]*National Center for Computational Sciences, Oak Ridge National Laboratory, P.O. Box 2008, Oak Ridge, Tennessee 37831, USA*
[2]*Laboratory for Atmospheric and Space Physics, CU, Boulder, Colarado 80309-256, USA*
[3]*NCAR, P.O. Box 3000, Boulder, Colorado 80307-3000, USA*
[4]*Space Sciences Laboratory, University of California, 7 Gauss way, Berkeley 94720, California, USA*
[5]*Institute for Chemical-Physical Processes-IPCF/CNR, Rende (CS) 87036, Italy*
[6]*Departamento de Física, Facultad de Ciencias Exactas y Naturales, Universidad de Buenos Aires and IFIBA, CONICET, Ciudad Universitaria, 1428 Buenos Aires, Argentina*

(Received 12 September 2014; accepted 3 May 2015; published online 19 May 2015)

We report results on rotating stratified turbulence in the absence of forcing and with large-scale isotropic initial conditions using direct numerical simulations computed on grids of up to 4096^3 points. The Reynolds and Froude numbers are, respectively, equal to $Re = 5.4 \times 10^4$ and $Fr = 0.0242$. The ratio of the Brunt-Väisälä to the inertial wave frequency, N/f, is taken to be equal to 4.95, a choice appropriate to model the dynamics of the southern abyssal ocean at mid latitudes. This gives a global buoyancy Reynolds number $R_B = ReFr^2 \approx 32$, a value sufficient for some isotropy to be recovered in the small scales beyond the Ozmidov scale, but still moderate enough that the intermediate scales where waves are prevalent are well resolved. We concentrate on the large-scale dynamics, for which we find a spectrum compatible with the Bolgiano-Obukhov scaling. This scaling is also found for geostrophically balanced initial conditions on a run at a lower resolution and hence lower $R_B \approx 4$. Furthermore, we confirm that the Froude number based on a typical vertical length scale is of order unity, with strong gradients in the vertical. Two characteristic scales emerge from this computation and are identified from sharp variations in the spectral distribution of either total energy or helicity. A spectral break is also observed at a scale at which the partition of energy between the kinetic and potential modes changes abruptly, and beyond which a Kolmogorov-like spectrum recovers. Large slanted layers are ubiquitous in the flow, in the velocity and temperature fields, with local overturning events indicated by small local Richardson numbers and strong localized vortex tangles . Finally, a small large-scale enhancement of energy directly attributable to the effect of rotation is also observed. © *2015 AIP Publishing LLC.* [http://dx.doi.org/10.1063/1.4921076]

I. INTRODUCTION

Rotating stratified flows are particularly important in the understanding of the dynamics of our planet and the Sun. Several of the key concepts needed in order to progress in predictions of the weather and of the global evolution of the climate depend crucially on a fundamental understanding of these flows. At different scales, different physical regimes become salient, and yet all scales interact. The nonlinear advection produces steepening, albeit slowly in the presence of strong waves. Thus, these fronts and turbulent eddies lead to enhanced dissipation and dispersion of particles and tracers, affecting the global energetic behavior of the atmosphere and climate systems, for example, for atmospheric synoptic scales and for oceanic currents, in the latter case modifying the meridional circulation. In the atmosphere, such effects on energetics can in turn impair assessments

of whether a given super-cell can spawn a tornado, and they affect both the evaluation of hurricane intensity and of climate variability. Rotating stratified turbulence (RST hereafter) thus plays a crucial role in the dynamics of the atmosphere and oceans, with nonlinear interactions—responsible for the complexity of turbulent flows—having to compete with the waves due to rotation and stratification.

A high-resolution direct numerical simulation (DNS) of homogeneous isotropic turbulence (HIT) on a grid of 4096^3 points, with Taylor Reynolds numbers of up to 1200 was performed a decade ago[1,2] (for the case of passive tracers and Lagrangian particles, see Refs. 3 and 4). For purely stratified flows, runs with comparable resolutions were presented recently in Ref. 5. In these simulations, energy cascades are found both in the vertical and the horizontal directions, with 1/3 of the dissipation coming from the former as in three-dimensional (3D) homogeneous isotropic turbulence and with a Kolmogorov spectrum in terms of the horizontal wavenumber at scales both larger and smaller than the Ozmidov scale. Part of the difficulty in determining spectral distribution among scales resides in the well-known fact[6] that the dynamics is anisotropic,[7] and thus, the isotropic spectrum should be replaced by an axisymmetric two-dimensional spectrum or by anisotropic correlation functions.

While these results were obtained for purely stratified flows, the effect rotation can have on stratified turbulence has been investigated by a number of authors in the Boussinesq framework.[8–14] The role played by the ratio N/f in these flows is relevant although, in some ways, poorly understood. In Ref. 8, it was shown that while stratification in the absence of rotation determines the vertical length scale $L_\parallel$ (basically, the buoyancy scale L_B associated with the thickness of vertical layers, with a Froude number based on this vertical length scale of order unity) and does so independently of the horizontal scale $L_\perp$, in RST, this scale has a more complex dependence on the buoyancy scale and on N/f, in which the Rossby number is the chief discriminating factor. However, specifically in the quasi-geostrophic limit, it is found[12] that $L_\parallel \propto fL_\perp/N$, with the proportionality, indeed, consisting of a function of Rossby number, as suggested in Ref. 8. We shall use this finding to help explain spectral features in our DNS.

In Ref. 9, elongated boxes were considered to study the emergence of a direct energy cascade in RST with a Kolmogorov spectrum in the horizontal direction, and it was shown that such is the case provided the Rossby number is greater than a critical value of ≈ 0.1. The case of large N/f ($\gtrsim 45$) was also considered, and the runs were performed using hyper-viscosity. The aspect ratio of the computational domain seems to play an important role in these studies and to influence the dynamics especially at unit Burger number $Bu = NL_\perp/fL_\parallel$. The linear regime of potential vorticity at $Bu = 1$ was analyzed in Ref. 15 (see also Ref. 16), and it was found that vortical modes dominate over waves at large scales, and that the parameter $\Gamma = fk_\parallel/(Nk_\perp)$ is relevant as a measure of the relative importance of terms in the linear part of the expression for potential vorticity: the two sources of dispersion become comparable when $fk_\parallel \sim Nk_\perp$. A more recent work on RST[17] deals with the emergence of helicity (vorticity-velocity correlations) in such flows, helicity being measured to be relatively strong in tornadoes and hurricanes,[18] and also being an important ingredient in the origin of large-scale magnetic fields in astrophysics.

As already mentioned, N/f is rather large in many applications. However, the case of RST with N/f of order unity (or slightly larger) is also of interest for geophysical flows. One example is the abyssal southern ocean at mid latitude,[19] which serves as a motivation for the present study and for which N/f is estimated to be between roughly 5 and 10. Flows with N/f ranging from 0.1 to 10 were analyzed in Refs. 10 and 11; all runs were spin-down with initial conditions at $k_0 \approx 10$. These authors stressed the importance of computing for long times compared to both the inertial and stratified periods of the waves, because of what are called slow modes, i.e., modes with zero wave frequency, as already emphasized in Ref. 14 (see also Ref. 20). In Ref. 14, it was also noted that energy builds up with time at small scales, the flow being strongly intermittent. Previous studies in the regime of moderate N/f also showed that the inverse cascade of energy to large scales is more efficient in the range $1/2 \le N/f \le 2$,[21] when wave resonances disappear.[14] Moreover, when forcing RST at intermediate to small scales, it can be shown that there is a clear tendency towards a $-5/3$ spectrum for the inverse cascade, as the Reynolds number increases for fixed parameters, together with the existence of a dual bi-directional energy cascade: to small scales with a positive

and constant energy flux and to large scales with again a constant but negative energy flux,[22,23] in accordance with oceanic data.[24]

Noticing the scarcity of high-resolution DNS for turbulence in the presence of both rotation and stratification to date and considering the geophysical relevance of flows with moderate values of N/f, we thus now analyze results from two runs with a numerical resolution using up to 4096^3 grid points at the peak of dissipation for the first one, and 512^3 points for an initially balanced run used to study the effect of varying the initial conditions. In Sec. II are given the equations, the numerical procedure, and the overall parameters. Sections III and IV provide, respectively, the temporal and spectral dynamics of the flow, Sec. V describes the physical structures that develop, and finally, Sec. VI offers a brief discussion and our conclusions.

II. NUMERICAL SETUP

A. Equations

The Boussinesq equations in the presence of solid body rotation for a fluid with velocity $\mathbf{u}$ and vertical velocity component w are

$$\frac{\partial \mathbf{u}}{\partial t} + \boldsymbol{\omega} \times \mathbf{u} + 2\boldsymbol{\Omega} \times \mathbf{u} = -N\vartheta \hat{e}_z - \nabla \mathcal{P} + \nu \nabla^2 \mathbf{u}, \tag{1}$$

$$\frac{\partial \vartheta}{\partial t} + \mathbf{u} \cdot \nabla \vartheta = Nw + \kappa \nabla^2 \vartheta, \tag{2}$$

together with $\nabla \cdot \mathbf{u} = 0$ assuming incompressibility. $\mathcal{P}$ is the total pressure, N is the Brunt-Väisälä frequency, $f = 2\Omega$ with Ω the rotation frequency, and ν and κ are the kinematic viscosity and scalar diffusivity (taken to be equal, for a Prandtl number equal to unity, $Pr = 1$). Finally, $\hat{e}_z$ is the unit vector in the vertical direction, which is in the direction of the imposed rotation and opposed to the imposed gravity, g; therefore, $\boldsymbol{\Omega} = \Omega \hat{z}$. Note that the normalized temperature fluctuation ϑ, that appears in the equations for momentum and mass conservation, derives from the standard Boussinesq formulation (see, e.g., Ref. 25) in terms of the density fluctuations about a stable background state,

$$\rho = -\overline{\frac{d\rho}{dz}} z + \rho', \tag{3}$$

by way of a change of variables,

$$\rho' = \frac{N \rho_0}{g} \vartheta. \tag{4}$$

Here, $N^2 = -(g/\rho_0)\overline{(d\rho/dz)}$ is a measure of the (constant) background stratification, ρ_0 is the mean density, ρ is the total density, and ρ' stands for the fluctuation around the background state. The "temperature" thus has units of velocity, and kinetic and potential energies are immediately comparable.

Equations (1) and (2) are then written in dimensionless units. A unit length scale and a unit r.m.s. velocity are used to dimensionalize all quantities. With this choice, for a characteristic velocity $U_0 = 1$ and a characteristic length $L_0 = 1$, the turnover time is $T_0 = L_0/U_0 = 1$, which we use as unit of time. Ω and N are then measured in units of the inverse of time T_0. The periodic domain has length $\lambda_0 = 2\pi$, resulting in integer wavenumbers and in a minimum wave number $k_{\min} = 2\pi/\lambda_0 = 1$.

The initial conditions for the velocity are centered on the large scales; all individual Fourier modes with $2 \le |\mathbf{k}|_0 \le 3$ are given an equal non-zero amplitude, with a total energy such that at $t = 0$, $u_{rms} = 1$. There is as much energy as in the three directions (isotropy is assumed), and the phases are chosen at random. In the first of the two runs considered ("run A"), we take $\vartheta(t = 0) = 0$, so the potential energy is initially zero ($E_P = \frac{1}{2}\langle \vartheta^2 \rangle = 0$). These initial values are standard in turbulence computations that focus on the nonlinear transfer of energy across scales. However, in order to check whether the specific initial conditions described above are responsible for the development of the features observed in this paper and in particular for Bolgiano-Obukhov (BO) scaling, we have

also performed an entirely different run ("run B") on a grid of 512^3 points in which "balanced" initial conditions are used. This run is described in Sec. IV B.

In the absence of dissipation ($\nu = \eta = 0$), the total energy $E_T = E_V + E_P$ is conserved, with $E_V = \frac{1}{2}\langle|\mathbf{u}|^2\rangle$ the kinetic energy. Besides the energy, rotating stratified flows also conserve the point-wise potential vorticity which can be defined as

$$P_V = f\partial_z\vartheta - N\omega_z + \omega\cdot\nabla\vartheta,$$

with $\omega = \nabla\times\mathbf{u}$ the vorticity. Because of the nonlinear term $\omega\cdot\nabla\vartheta$ in the expression of P_V, its $\mathcal{L}_2$ norm is quartic and thus it is not conserved by each triadic interaction in a truncated ensemble of modes. The extent to which this is relevant to the dynamical evolution of the flow is not entirely known, but several studies for shallow water[26] or the Boussinesq equations[27–29] assess the relative importance of the different contributions to P_V, with the general assumption that the high-order terms can be neglected when the waves are strong enough, i.e., at small Froude and/or Rossby numbers. By contrast, for the particular case of stable stratification, it was hypothesized in Ref. 29 that when the buoyancy Reynolds number R_B is large enough, the nonlinear term in P_V affects the dynamics, becoming important at the same time as Kelvin-Helmholtz instabilities develop in the flow.

When linearizing primitive equations (1) and (2) in the absence of dissipation, one obtains inertia-gravity waves of frequency

$$\omega_k = k^{-1}\sqrt{N^2k_\perp^2 + f^2k_\parallel^2}, \tag{5}$$

with $k = \sqrt{k_\perp^2 + k_\parallel^2}$, $k_\perp = \sqrt{k_x^2 + k_y^2}$, and $k_\parallel = k_z$, respectively, the total, horizontal (or perpendicular), and vertical (or parallel) wavenumbers (see, e.g., Refs. 27 and 30).

Fourier spectra will be built-up from their axisymmetric counterparts defined from the two-point one-time velocity covariance $U(\mathbf{k})$ (see, e.g., Ref. 31)

$$e_V(|\mathbf{k}_\perp|,k_\parallel) = \sum_{\substack{k_\perp\le|\mathbf{k}\hat{\mathbf{x}}|<k_\perp+1\\ k_\parallel\le k_z<k_\parallel+1}} U(\mathbf{k}) = \int U(\mathbf{k})|\mathbf{k}|\sin\theta d\phi = e(|\mathbf{k}|,\theta) = e(k,\theta), \tag{6}$$

here ϕ is the longitude with respect to the k_x axis and θ is the co-latitude in Fourier space with respect to the vertical axis. The function $e_V(\mathbf{k}_\perp, k_\parallel = 0)$ may be regarded as the spectrum of two-dimensional (2D) modes, having no vertical variation. Note that for an isotropic flow, at a given point $\mathbf{k}$ in wavenumber space, the ratio of the axisymmetric spectrum $e_V(|\mathbf{k}_\perp|,k_\parallel)$ to the isotropic spectrum is $\sim 1/|\mathbf{k}|$ because the size of the volume element in the isotropic case contains an additional (integrating) factor of $|\mathbf{k}|$ compared to the axisymmetric case. Hence, if the axisymmetric spectrum behaves as $k_\perp^{-\alpha}$, then the corresponding isotropic scaling will be $k^{-\alpha+1}$. The spectrum $e_V(|\mathbf{k}_\perp|,k_\parallel)$ can also be decomposed into the kinetic energy spectrum of the horizontal components (velocity components u and v) and of the vertical kinetic energy (velocity component w),

$$e_V(|\mathbf{k}_\perp|,k_\parallel) = e_\perp(|\mathbf{k}_\perp|,k_\parallel) + e_\parallel(|\mathbf{k}_\perp|,k_\parallel). \tag{7}$$

In the following, we will also consider the reduced perpendicular spectrum,[32]

$$E_V(k_\perp) = \Sigma_{k_\parallel} e_V(\mathbf{k}_\perp,k_\parallel), \tag{8}$$

the reduced parallel spectrum $E_V(k_\parallel)$ (which has a sum over $k_\perp$), and the spectrum representing the perpendicular energy of the strictly 3D modes,

$$E_{3D}(k_\perp) = E_V(k_\perp) - e_{V,\perp}(\mathbf{k}_\perp, k_\parallel = 0). \tag{9}$$

Similar definitions hold for the helicity and potential energy spectra, $h_V(\mathbf{k}_\perp,k_\parallel)$ and $e_P(\mathbf{k}_\perp,k_\parallel)$, their reduced forms, $H_V(\mathbf{k}_\perp)$ and $E_P(\mathbf{k}_\perp)$, as well as their 3D expressions (i.e., the perpendicular spectra of the 3D modes), $H_{V,3D}(\mathbf{k}_\perp)$ and $E_{P,3D}(\mathbf{k}_\perp)$. These spectra will be analyzed in Sec. IV.

B. Specific numerical procedure

The code used in this paper is the Geophysical High Order Suite for Turbulence (GHOST), which is fully parallelized using a hybrid methodology.[33] It uses parallel multidimensional FFTs in a pseudo-spectral method for 2D and 3D domains on a regular structured grid and can solve a variety of neutral-fluid partial differential equations, as well as several that include a magnetic field. Boundary conditions are periodic, and the time-integration is performed using a Runge-Kutta algorithm up to 4th-order with double precision arithmetic. The code uses a "slab" (1D) domain decomposition among Message Passing Interface (MPI) tasks, and OpenMP threads provide a second level of parallelization within each slab or MPI task. The code demonstrates good parallelization to more than 100 000 compute cores.

In order to achieve a high resolution at peak of dissipation when gradients of variables are the strongest, we have implemented a "bootstrapping" procedure in which we start the simulation at a lower resolution until the *dynamic range* of the energy spectrum decreases to some fiducial value. Here, by dynamic range, we refer to the ratio of the energy at the peak of the spectrum, to the energy at the largest available wavenumber at a given resolution. When the lower threshold ($\approx 10^{-10}$) is reached, we increase the resolution and continue running until the dynamic range of the DNS at the new resolution decreases again to the fiducial value, repeating the process. Bootstrapping requires that a field at a reduced resolution be "padded" spectrally with zeros from its largest allowed wavenumber to the larger wavenumber allowed at the next (higher) resolution. This is handled in a processing step before the next highest resolution DNS is computed. This bootstrapping procedure was recently implemented, tested, and used in the context of ideal magnetohydrodynamics.[34]

We thus began with a 1536^3 run up to $t = 2$ (note that all times henceforth are given in units of evolutionary time, unless stated otherwise), then doubled the resolution on a grid of 3072^3 grid points up to $t = 5$, and then completed the run on the grid with 4096^3 points. The maximum resolved wavenumber using a classical 2/3 de-aliasing rule is $k_{max} = N/3 = 1365$, with the length of the box corresponding to wavenumber $k_{min} = 1$. The viscosity and scalar diffusivity were chosen to be the same for these three successive runs, each run representing the evolution of the same physical problem at earlier times. The time step for each was chosen on the basis of the highest resolution considered in order to minimize time stepping errors at lower resolution. The first bootstrapping was done at the end of the inviscid phase before the small scale structures that can dissipate energy develop substantially.

The run on the intermediate grid of 3072^3 points was also pursued to later times ($t_{max} = 6.7$); this enabled us to inspect the convergence of the overall statistics at the same evolutionary times.

C. Dimensionless parameters

The dimensionless numbers associated with the Boussinesq equations are defined as

$$Re = \frac{U_0 L_0}{\nu},\ Fr = \frac{U_0}{L_0 N},\ Ro = \frac{U_0}{L_0 f},\ Pr = \frac{\nu}{\kappa}, \tag{10}$$

where U_0 and L_0 are, respectively, a characteristic velocity and length scale. A number of studies have shown, at least in the absence of rotation, that the buoyancy Reynolds number, R_B, needs to be large enough for vigorous turbulence to develop in the small scales (see, for example, the review in Ref. 35 and references therein). In fact, in the rotating and stratified case, the combined effect of turbulent eddies and waves can be encompassed in the buoyancy and inertial Reynolds numbers, R_B and R_Ω, respectively, defined via

$$R_B = ReFr^2,\ R_\Omega = ReRo^2. \tag{11}$$

Indeed, at $R_B = 1$, the Ozmidov scale

$$\ell_{OZ} = 2\pi/k_{OZ} = 2\pi\sqrt{\varepsilon_V/N^3}, \tag{12}$$

at which isotropy recovers in a purely stratified flow, is comparable to the dissipation (or Kolmogorov) scale, $\ell_\eta = 2\pi/k_\eta = 2\pi(\nu^3/\varepsilon_V)^{1/4}$, where $\varepsilon_V = |dE_V/dt|$ is the rate of dissipation of kinetic energy. For $R_B \gg 1$, a Kolmogorov range, typical of isotropic and homogeneous turbulence,

develops before dissipation can become effective. Similarly, in a purely rotating flow, one can similarly define the Zeman scale $\ell_\Omega = 2\pi/k_\Omega = 2\pi\sqrt{\varepsilon_V/f^3}$. For $R_\Omega \gg 1$, isotropy recovers beyond this scale as shown in Ref. 31. Resolving such characteristic scales in a DNS may effect the resulting dynamics and energy distributions. This has been examined in Refs. 36–38 at lower resolutions (with linear resolution in at least one direction up to 2048 points) with regard to both the Ozmidov scale (Eq. (12)) and the so-0called buoyancy scale,

$$L_B = 2\pi U_0/N, \tag{13}$$

which gives the characteristic thickness of the vertical layers in a stratified system. A similar characteristic length scale can be defined based on the rotation rate, f. We consider these scales in Sec. IV; in Sec. IV C, we provide a modification of L_B due to rotation that is suggested by our results.

Note these length scales are written for a domain with dimensionless length of 2π, such that $k = 2\pi/\ell$ is the wavenumber; a wavenumber $k = 1$ for a given characteristic lengthscale thus corresponds to the largest scale in the domain $\ell = 2\pi$. In other words, all length scales are measured in terms of the overall dimension of the flow (and no such 2π factor appears in the equivalent definition in terms of wavenumber).

As mentioned in the Introduction, a variety of other dimensionless combinations of relevant physical parameters can be defined for rotating stratified turbulence, beyond those written in Eq. (10). In fact, one of the central limitations to a better understanding of such flows is the need to unravel what the key parameters are that govern the dynamics. As an example, beyond the Reynolds, Froude, Rossby, and Prandtl numbers, one can also consider the ratio N/f or the Froude number based on a characteristic vertical length scale,

$$F_z = U_0/(\ell_Z N).$$

The partition of energy between kinetic and potential modes can be measured by their ratio, E_V/E_P, which is one possible definition of the Richardson number. Another definition is simply to measure the relative strength of the buoyancy to the inertial forces or

$$Ri = 1/Fr^2.$$

However, in order to emphasize the role of the development of small scales in mixing, we consider the standard gradient Richardson number in terms of the primitive variables used in Eq. (1),

$$Ri_g = -\frac{g}{\rho_0}\partial_z\rho/(\partial_z u_\perp)^2 = N(N - \partial_z\vartheta)/(\partial_z u_\perp)^2, \tag{14}$$

where we have used expansion Eq. (3) and definition Eq. (4). This form suggests that a sufficiently large vertical gradient locally leads to negative values of Ri_g, which is consistent with the intuitive picture of overturning when a denser parcel of fluid lies atop a less dense parcel.

D. Parameters and general characterization for 4096^3 run

We use $N/f = 4.95$ with $N = 13.2$ and $\Omega = f/2 = 1.33$ (thus, $f = 2.67$). The viscosity is chosen to have the simulation well resolved: $\nu = 4 \times 10^{-5}$; the time step is $dt = 1.5 \times 10^{-4}$. In dimensionless units, the resulting overall energetics of the flow lead to several scales that are of interest and to a characterization of the flow in terms of the dimensionless parameters. Considered at the peak of enstrophy, the characteristic velocity is $U_0 \approx 0.83$ and the integral length scale, computed from $L_{int} = 2\pi \int E_V(k)dk/\int kE_V(k)dk \approx 2.6$, very close as expected to the scale at which the energy spectrum initially peaks, namely, $L_0 = 2\pi/k_0 \approx 2.5$. This gives an eddy turn-over time of $\tau_{NL} = L_{int}/U_0 \approx 3.1$. The dissipation rate of the kinetic energy is taken from an evaluation of the kinetic enstrophy averaged over the interval $t \in [5.3, 5.7]$ about the peak of dissipation: $\varepsilon_V = \nu\langle|\omega|^2\rangle \approx 0.0123$ (see Fig. 1(a)). Note that in the isotropic case, $\varepsilon_V = \epsilon_K = U_0^3/L_{int} \approx 0.22$, but this relation does not hold in the highly anisotropic system we are investigating. Rather, we can take an estimate coming from weak turbulence, namely, $\epsilon_K * Fr \approx 0.005$, within a factor of two of the measured rate of energy dissipation. The Kolmogorov dissipation wavenumber is computed at

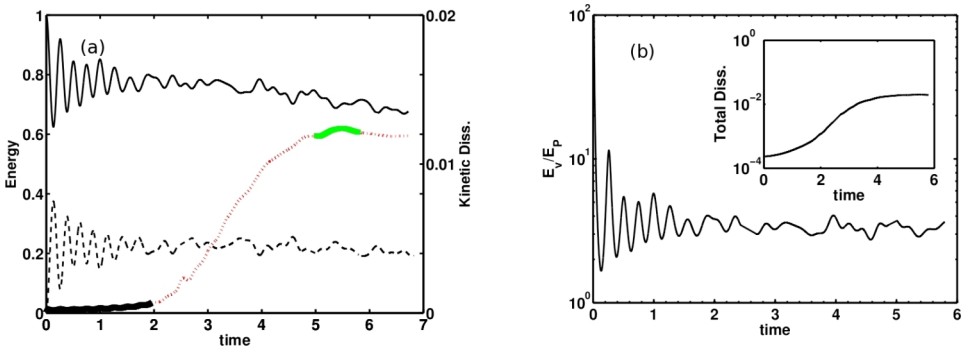

FIG. 1. (a) Temporal variation of kinetic (solid line) and potential (dashed line) energies and of the total energy dissipation rate for run A with a dotted (red) line for the run using the 3072^3 grid which evolved until $t = 6.7$. The squares (green) represent the run performed on the grid of 4096^3 points, evolved for $5 \le t \le 5.88$ (i.e., for a duration of ≈77 gravity wave periods), and the triangles (black) indicate the early time run on a grid of 1536^3 points. All three runs have the same physical parameters and time step. (b) Temporal variation of the ratio of kinetic to potential energy. In the inset is the total energy dissipation in lin-log coordinates.

the peak of dissipation to be $k_\eta \approx 660$. The Zeman and Ozmidov wavenumbers are therefore found to be, respectively, $k_\Omega \approx 39$ and $k_{OZ} \approx 431$. The buoyancy wavenumber is $k_B = 2\pi/L_B \approx 16$; the lack of scale separation between k_Ω and k_B suggests that it will be difficult to distinguish as separate effects those due to rotation and those due to stratification. The Reynolds number is thus found to be $Re \approx 5.4 \times 10^4$, the Froude number is $Fr \approx 0.0242$, and the Rossby number is $Ro \approx 0.12$. Consequently, the buoyancy and rotational Reynolds numbers are $R_B \approx 32$, and $R_\omega \approx 775$. The Richardson number is determined to be $Ri \approx 1700$, so the flow is, indeed, found to be strongly stratified.

Finally, we can define a Taylor Reynolds number as $R_\lambda = U_0\lambda/\nu$, with $\lambda = 2\pi[\int E_V(k)dk / \int k^2 E_V(k)dk]^{1/2}$ the Taylor scale. In classical HIT, R_λ measures the degree of development of small scales. At peak of dissipation, $\lambda \approx 0.31$, leading to a rather large $R_\lambda \approx 6400$, quite high compared to similar computations in HIT (e.g., $R_\lambda \approx 1200$ in a HIT run at similar grid resolution[1,2]). This is linked to the fact that, in the presence of strong waves, the transport of energy to small scales is hindered and not as efficient, and the energy spectrum becomes steeper at least at large scales, resulting in a larger Taylor scale for the same viscosity. It is worth noticing that in the atmosphere, the Taylor Reynolds number is estimated to be $R_\lambda \approx 20\,000$, and it may be the case that realistic simulations of stratified and rotating atmospheric turbulence may be feasible in the near future as a result of this effect. Finally, note also that the value of R_λ puts the present computation above the different thresholds in R_λ identified in Ref. 39 for various instabilities to develop, as, e.g., for the growth of vertical shear and the growth of vertical energy.

When the dimensionless numbers obtained in the simulation at the peak of dissipation given above are now dimensionalized using the characteristic length and velocity of the Southern Abyssal Ocean at mid latitudes, i.e., with $L_o = 1000$ m (corresponding to the peak of energy input in the ocean from bathymetry[40]) and $U_o = 0.024$ m s^{-1}, as measured, for example, in the Drake passage,[19] we obtain kinematic viscosity and scalar diffusivity, respectively, of $\nu_o = \kappa_o = 4.5 \times 10^{-4}$ m^2 s^{-1}, too large by roughly two orders of magnitude. The corresponding overall effective energy dissipation rate, obtained from the dimensionless value measured directly in the simulation, would be $\epsilon \approx 1 \times 10^{-9}$ m^2/s^3. This value can be compared with measurements in the southern ocean.[41] As a further comparison, note also that this value for the dissipation rate is significantly smaller than atmospheric measurements, which indicate $\epsilon \approx 10^{-6}$ m^2 s^{-3} at intermediate altitude and at scales between 3 and 600 km.[42]

With a rotation frequency of $\Omega = 10^{-4}$ s^{-1}, our choice of parameters leads to a Brunt-Väisälä frequency of $N \approx 10^{-3}$ s^{-1} and $Fr \approx 0.024$, corresponding to the parameters of the run described above. The buoyancy scale is 150 m, the Ozmidov scale is 4 m, and the Kolmogorov dissipation scale is around 0.15 m. This last value is too large, because the viscosity is too large and the numerical resolution is still insufficient. Slightly different values can be taken of course, such as $N \approx 7 \times 10^{-4}$ and $f \approx 1.5 \times 10^{-4}$ (thus, $N/f \approx 4.67$) as done in Ref. 19. Note also that another

element lacking in our simulation is the interaction with a larger-scale (mean) flow, say at the scale of several hundred kilometers, together with proper boundary conditions in the vertical.

III. OVERALL TEMPORAL DYNAMICS FOR RUN A

We now examine in more detail the overall temporal evolution of large-scale features in the simulation with the largest resolution. Figure 1(a) displays the kinetic and potential energy as a function of time (solid and dashed lines, respectively), as well as the dissipation of the kinetic energy, $\nu \langle \omega^2 \rangle$, whereas in Fig. 1(b) is given the ratio of kinetic to potential energy, and in the inset the total energy dissipation in lin-log coordinates. The three distinct intervals with bootstrapping are identified in the dissipation in (a) with different symbols: the thick line starting at t = 0 is done on a grid of 1536^3 points, the thin dotted line going to $t_{max} \approx 6.7$ is performed on a grid of 3072^3 points, and the short thick line around t = 5 is the run on the largest grid of 4096^3 points.

Easily identifiable initial oscillations due to the waves prevail at early times; these oscillations, stronger and thus more visible at large scale in the evolution of the energy, are due to inertia-gravity waves and their irregularity is linked with nonlinear coupling which, at that Reynolds number, is sizable. However, the ratio of kinetic to potential energy remains relatively constant on average throughout the run after the initial phase, at a value close to 3. This initial phase is essential, since, even though our initial conditions have $E_P = 0$ (and random phases for the velocity at large scale), the gravity waves provide a source of organized potential energy for the next temporal phase when nonlinearities arise and constant-flux self-similar spectral scaling develops (see Sec. IV). The kinetic energy starts to decay rather slowly as small scales have been formed. By the end of the run, the dissipation has reached a plateau and the flow is fully developed. When examining the temporal evolution of the energy and dissipation for the flows computed on 3072^3 and 4096^3 points, no differences are visible, indicative of a converged simulation and of a well-resolved flow. At the peak, $\varepsilon_V \approx 0.0123$, and the dissipation of potential energy is $\varepsilon_P = \kappa \langle |\nabla \vartheta|^2 \rangle \approx 0.0077$ (not shown). The start of the growth of the dissipation at $t \approx 2$ coincides with the development of nonlinear eddy interactions and with a lesser amplitude in the oscillations which marks exchanges between the kinetic and potential energies; this time is slightly shorter than the eddy turn-over time built on the saturated values of the integral length scale $L_{int} \approx 2.5$ (see Fig. 2) and the r.m.s. velocity, $U_0 \approx 0.83$ (see Sec. II D).

In Fig. 2 are given the temporal evolution of the ratio of the $\mathcal{L}_2$ norms (volume averages) of the vertical to horizontal kinetic energy, as well as a characteristic vertical length scale defined as

$$\ell_z = [\langle u_\perp^2 \rangle / \langle (\partial_z u_\perp)^2 \rangle]^{1/2}. \tag{15}$$

Note that ℓ_z can be viewed as a vertical Taylor scale, since it is based on vertical gradients of the (horizontal) velocity. As expected, the horizontal kinetic energy dominates over the vertical

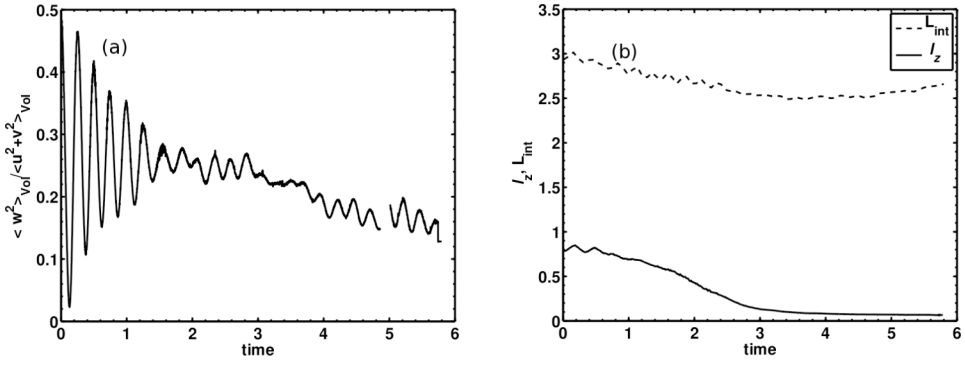

FIG. 2. Temporal evolution for run A on a 4096^3 grid of (a) the ratio of the volume averaged vertical to horizontal kinetic energy, $\langle w^2 \rangle / \langle u^2 + v^2 \rangle$, and (b) the vertical length scale ℓ_z defined in Eq. (15), which is characteristic of vertical shear layers. The integral scale L_{int} is also provided (dotted line) in order to compare with ℓ_z.

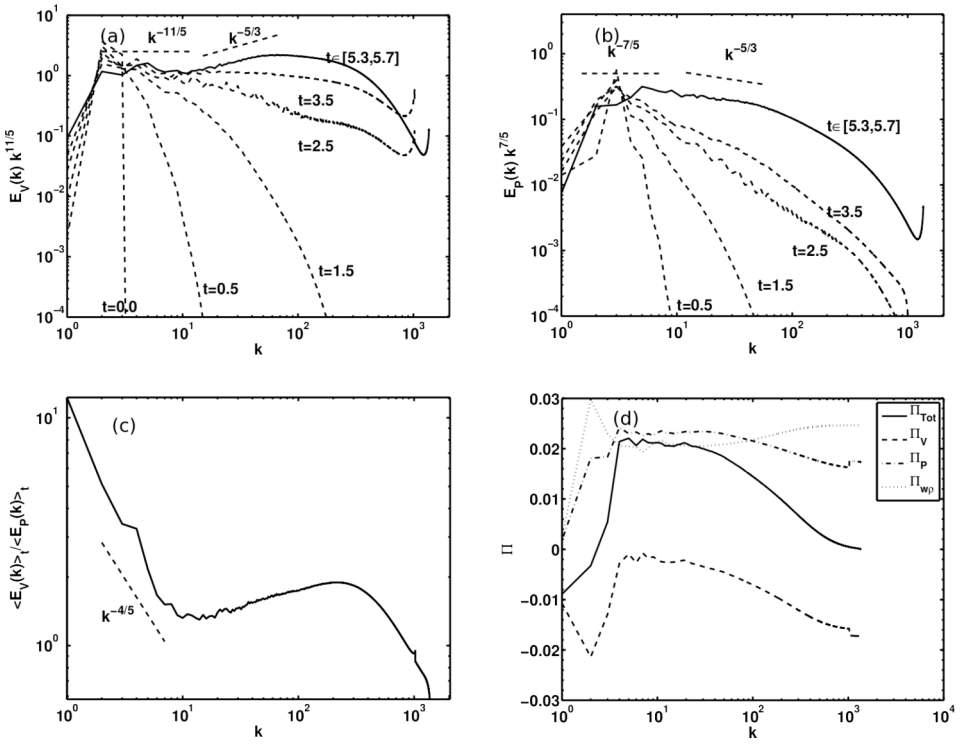

FIG. 3. ((a) and (b)) High-resolution isotropic spectra for run A done on a grid of 4096^3 points for the (a) kinetic energy compensated by an $11/5$ power law and (b) potential energy compensated by a $7/5$ power law, averaged over the time interval $t \in [5.3, 5.7]$ corresponding to the peak in enstrophy (solid lines). In dashed lines are spectra at earlier times, as indicated by the labels. (c) Ratio of kinetic to potential energy spectra averaged over the same time interval; note the clear transition around $k \approx 12$ and a scaling close to $k^{-4/5}$. (d) Total energy flux and, separately, kinetic and potential fluxes, as well as the buoyancy flux term obtained from Eq. (18). All fluxes are averaged over the same time interval. Note the negative total flux at large scale (stronger in fact for the kinetic energy flux), indicative of the effect of rotation.

at all times, by a factor close to 4, and increasingly so after the peak of enstrophy. The vertical length-scale, of order unity to start with, undergoes a steady decrease and stabilizes as the peak of enstrophy is approached; it is one order of magnitude smaller at peak of dissipation when compared with its initial value. Considering now the vertical Froude number based on this vertical shearing length, $F_z = U_0/(N\ell_z)$, we find $F_z \approx 0.9 \lesssim 1$ at the latest time of the run. This value for F_z is predicted for strongly stratified flows from the self-similarity analysis in Ref. 8, if ℓ_z is taken to be the vertical scale of the dynamics, since, in this case, it is shown that $\ell_z \sim U_0/N$. One can contrast the anisotropy arising from rotation and stratification and say that the flow is fully turbulent but in an anisotropic manner,[7] although it still does feel the effect of rotation, as can be seen in Fig. 3(d), with a negative energy flux at large scale, more strongly so in the kinetic energy component.

IV. SPECTRAL BEHAVIOR

A. Evidence for a large-scale Bolgiano-Obukhov scaling in run A on a 4096^3 grid

In Fig. 3, we show for run A and with solid lines several isotropic spectra, which are all averaged around the peak of dissipation in the interval $t \in [5.3, 5.7]$ (see Fig. 1(a)). The isotropic kinetic (Fig. 3(a)) and potential (Fig. 3(b)) energy spectra are compensated by a $k^{-11/5}$ power law, and a reference line is provided for a Kolmogorov-like $k^{-5/3}$ law. The Kolmogorov-like law is compatible with the scaling of the spectrum observed at smaller scales, for $k_c \le k \le 100$ with $k_c \approx 12$; note that this value is close to the buoyancy wavenumber $k_B \approx 16$ but may nevertheless differ from it (see below). Early time spectra are also given, in dashed lines and with the time labeling the curves. This

allows to see the temporal evolution of spectrum from initial conditions centered on $k_0 \in [2, 3]$. We observe that by $t \approx 2.5$, the spectra have gained substantial excitation in the small scales and that by $t \approx 3.5$, they are almost completely developed; this time interval ($2.5 \leq t \leq 3.5$) corresponds to the progressive damping of the substantial oscillations observed in the temporal evolution of the energy at earlier times (see Fig. 1). Figure 3(b) gives the potential energy spectra for the same times (except for $t = 0$ where $E_P = 0$).

At larger scales, steeper spectra are observed ($E_V(k) \sim k^{-11/5}$, $E_P(k) \sim k^{-7/5}$), with values of ≈ -2.2 and ≈ -1.4, respectively, being computed from least-squares fits on the interval $k \in [2, 14]$. Note that spectra with a power-law index close to -2 were found in Ref. 43 for N/f varying from 4 to 32, and observations in the ocean also indicate values that are similar and in fact closer to 2.5.[24]

These spectral indices can be interpreted in the following way. A characteristic feature of stratified flows is the role that the density or temperature fluctuations can play in the dynamical evolution as well as in the scale distribution of the energy, with the scalar being either passive (as it would be in the purely rotating case) or active. In this context, one can invoke a dimensional argument to explain the large-scale spectral distribution, namely, the BO scaling (Refs. 44 and 45) derived for purely and stably stratified turbulence. This scaling is obtained under the assumption that the source of energy at large scale is contained in the buoyancy, or in the potential modes, with nonlinear transfer rate $\varepsilon_P = |dE_P/dt|$ assumed constant and with a negligible advection term in the momentum equation. Since ϑ in the primitive equations written in Eq. (2) has the dimension of a velocity, we have to re–introduce the physical dimension of the buoyancy flux in terms of length and time, i.e., $[\epsilon_P] = [L^2T^{-5}]$; similarly, one can use $\varepsilon_P N^2$ for the constant flux. This then leads to (see Ref. 46 for a review)

$$E_V(k) = B_V \varepsilon_P^{2/5} k^{-11/5}, \; E_P(k) = B_P \varepsilon_P^{4/5} k^{-7/5}, \tag{16}$$

with Kolmogorov-like constants B_V and B_P.

In the BO phenomenology, the scalar actively modifies the velocity field. Note that the Coriolis force due to rotation does not contribute to the energy balance but only to an angular redistribution of energy favoring negative flux to large scales and thus does not perturb the dynamics leading to the BO scaling. When examining the fluxes in the equation for the kinetic energy within this framework, the advection and the buoyancy terms both scale as $r^{4/5}$: they balance each other while not being constant in the inertial range and diminish in amplitude as scales become smaller. On the other hand, the advection term in the equation for the potential energy is constant, by construction of this phenomenological argument. Indeed, the Bolgiano-Obukhov phenomenology derives from the idea that at large scales, the nonlinear advection term in the momentum equation is not strong enough in the direct cascade to small scales, and the only available source for kinetic energy is therefore that coming from the scalar fluctuations. Requiring that the kinetic and potential energy spectra depend only on the dimensional buoyancy flux, ε_P, and wavenumber, k, leads to the above spectra.

From the fits to the kinetic and potential energy spectra, we have found that the constants are $B_V \sim 7$ and $B_P \sim 6$, which are higher than would be expected based on a Kolmogorov phenomenology in three dimensions, but in fact close to two-dimensional values for the inverse cascade (see Ref. 47 for review); this may be due to the fact that we observe a small inverse transfer of kinetic energy (see the energy fluxes in Fig. 3(d)).

We can evaluate the wavenumber, K_{BO}, at which the transition from a Bolgiano-Obukhov to a Kolmogorov spectrum $E_V(k) = c_K \varepsilon_V^{2/3} k^{-5/3}$ takes place, in the framework of the BO scaling, by equating the two kinetic energy spectra at that scale. This leads immediately to

$$K_{BO}(B_V/c_K)^{15/8} \varepsilon_P^{3/4} \varepsilon_V^{-5/4}. \tag{17}$$

For ε_V, we select the value of the kinetic energy flux to be that represented by the rate at which kinetic energy is dissipated at the smallest scales. Averaging the dissipation rate (Fig. 1(a)) over the interval $t \in [5.3, 5.7]$ about the peak in enstrophy yields $|\varepsilon_V| \approx 0.0123$. The value for ε_P is taken to be value of the potential energy dissipation rate, $\varepsilon_P \approx 0.0077$, averaged over the same time interval, as mentioned in Sec. III. Finally, we measure c_K directly from the time-averaged spectrum in Fig. 3(a) just after the start of the $k^{-5/3}$ region at $k = 15$, to find $c_K = 5.4$. This too is high for a three dimensional isotropic simulation, but within the range of values cited in Ref. 47

for two dimensional inverse cascades. Note also that the range we are using is at scales greater than the Zeman scale ($k < k_\Omega$), where rotation is still expected to influence the dynamics. Using these values for the spectral fluxes and for the Kolmogorov constants, we find $K_{BO} \approx 10$, very close to the observed value of $k_c \approx 12$.

There is evidence of Bolgiano-Obukhov scaling in two-dimensional laboratory experiments of convective flows,[48] as well as in three dimensions.[49] In this latter case, the way the BO scaling was unraveled was to perform conditional structure functions in order to select the locations of the flow in which the Bolgiano-Obukhov length $L_{BO} = 2\pi/K_{BO}$ is sufficiently smaller than the characteristic size of the experiment L_0, by doing a local analysis of the potential energy dissipation rate on which L_{BO} is based, and the BO scaling was obtained far from the boundaries. Another way in which the Bolgiano-Obukhov scaling can be found is to consider an aspect ratio for the fluid which is small, a condition easily fulfilled by the atmosphere and the ocean. In Ref. 50, it is shown using direct numerical simulations in tall boxes that the occurrence of the BO scaling is linked to the appearance of an inverse cascade of energy in such fluids due to a quasi-bi-dimensionalization imposed by the geometry.

In our simulations, rotation induces a quasi-bi-dimensionalization as well as a marked inverse transfer (note that inverse energy cascades and transfers are commonly observed in RST flows when forced at an intermediate scale, see, e.g., Refs. 14, 22, and 23). A recent analysis of a three-dimensional DNS of a non-rotating stratified unbounded turbulent flow also finds BO scaling for the spectra in the stably stratified (no rotation) regime for lower levels of stratification and at lower Reynolds number than those presented here.[51] There are also indications that the BO scaling has been observed in stably stratified flows in the atmosphere,[52] and specifically in the surface layer[53] and in the troposphere.[54] These latter works stress the role of anisotropic structures developing because of the imposed forces (rotation and gravity) and the ensuing breaking of the isotropic Kolmogorov law.

We now show in Fig. 3(c) the ratio of the kinetic and potential energy spectra which were averaged over the time interval corresponding to the peak of enstrophy, the BO prediction being indicated as a dashed line with a $-4/5$ slope. This scaling seems to hold at large scales, up to $k \approx 12$ for the velocity, and on a shorter range for the temperature field (see Fig. 3(b)) Finally, Fig. 3(d) displays several fluxes. The (forward) flux of total energy (solid line) is approximately constant, at a level of ≈ 0.022 in these two identified ranges, indicative of a classical turbulent cascade. Note also that it becomes negative (reaching ≈ -0.0085) at scales larger than the scale of the initial conditions; it can be expected, therefore, that, in the presence of forcing, a small inverse cascade may develop, as observed in Ref. 28 and as it does when the forcing is placed at smaller scale (see, e.g., Refs. 21, 22, and 55).

We show finally in Fig. 3(d) the energy flux decomposed into its kinetic (dashed) and potential (dashed-dotted) components, $\Pi_{V,P}$, as well as the buoyancy flux, $\Pi_{w\vartheta}$, (dotted line), defined in wavenumber space as

$$\Pi_{w\vartheta}(k) = \sum_{k'=0}^{k'=k} \sum_{k'<|k''|<k'+1} \Re(\hat{w}(\mathbf{k}'')\hat{\vartheta}(\mathbf{k}'')^*), \tag{18}$$

where $\hat{w}(\mathbf{k})$ and $\hat{\vartheta}(\mathbf{k})$ are the Fourier coefficients for the vertical velocity and the scalar, respectively. The first two fluxes, $\Pi_{V,P}$, correspond to a scale–by–scale analysis of the two non-linear flux terms, $\vartheta\mathbf{u}\cdot\nabla\vartheta$ and $\mathbf{u}\cdot[\mathbf{u}\cdot\nabla]\mathbf{u}$, whereas the buoyancy flux concerns the linear modal energetic exchanges between the velocity and density fluctuations. The sum of the kinetic dissipation at its peak (see Fig. 1(a)) plus the kinetic energy flux, $\Pi_v(k=1) \approx -0.01$ is ≈ 0.0024, which is in excellent agreement with the nearly constant value of Π_v in the region $k \in [4, 20]$ is seen in this figure. Furthermore, it can be seen that, as hypothesized in the BO phenomenology, the potential flux to small scales is dominant, constant, and positive for a wide range of scales. The kinetic flux has a strong peak at wavenumbers smaller than k_0. It is in fact negative throughout the wavenumber range around the peak of enstrophy, but close to zero in the Bolgiano-Obukhov range, again as hypothesized in the BO phenomenology; this is likely due to the fact that the buoyancy flux acts as a source of energy for the velocity in a wide range of scales.

We present the time average of $\Pi_{w\vartheta}$ in Fig. 3 ((d), dotted curve), where it is seen that it is, in fact, comparable to the total energy flux and can serve potentially as a kinetic energy source. We note that large temporal fluctuations in the buoyancy flux are observed; they correspond to gravity waves directly affecting vertical motions.

The agreement of the spectral scalings with the BO phenomenology, as well as the compatibility between the K_{BO} computed with measured data and the observed k_c offer compelling evidence of BO scaling in this decaying strongly stratified, weakly rotating DNS. The problem remains, however, that there is little scale separation for $k < K_{BO}$ before a different dynamics dominates at larger wavenumbers. A parametric study at high Reynolds number, achieved by varying the buoyancy force may help to determine the likelihood of such scaling laws in unbounded stratified turbulence; conditional averaging[49] may be effective for such a study.

Another factor could be taken into consideration, in principle, to elucidate the scaling observed in our run, namely, that of the effect of large-scale shear. While shear is not imposed in our run, strong shear layers develop in the vertical in stably stratified flows, even in the presence of rotation (in which case they are slanted, see Figs. 8–10). Shear is created locally and leads to strong instabilities (see Fig. 10(c) below), so we must consider its effect on spectral behavior. A shear scaling leads to the following spectra:

$$E_V(k) \sim \epsilon_V^{1/3} S k^{-7/3},\ E_P(k) \sim \epsilon_P \epsilon_V^{-1/6} S^{-1/2} k^{-4/3},$$

where S is the shear rate (which can also be expressed in terms of a shear length scale).[46] In this case, the scalar is passive, and the ratio of the two spectra varies as k^{-1}, so the spectral indices are close to those that we find in our results. However, we have argued in part by considering $\Pi_{w\vartheta}$ (Eq. (18)) and its magnitude relative to the total energy flux that the scalar field is not passive. Furthermore, the excellent agreement of the observed spectral indices (if in a short inertial range) and the accord between the observed break in the spectra at k_c and the computed K_{BO} seem to suggest that BO scaling is more likely; this may be a first instance of such a scaling in a DNS of high Reynolds number strongly stably stratified unbounded flows in the presence of rotation (see Ref. 51, as well as Refs. 57 and 58 for the purely stratified case).

B. Balanced initial conditions

The analysis presented in Sec. IV A raises the question of whether this finding of a Bolgiano-Obukhov scaling depends on initial conditions. In particular, it is natural to ask whether a large-scale geostrophic and hydrostatic balance such as that observed in the atmosphere would also lead to the same result. In this context, we have also performed a run on a grid of 512^3 points (run B), with initial conditions for which there is both geostrophic and hydrostatic balance. Specifically, the initial vertical velocity is taken equal to zero, $w = 0$, and the horizontal components of the velocity are initialized from a stream function, ϕ, that is three dimensional and isotropic at large scales with random phases (compare with run A in Sec. II A), such that $u = \partial_y \phi$ and $v = -\partial_x \phi$ (so that $\nabla \cdot \mathbf{u} = 0$). Neglecting the nonlinear and dissipative terms in Eq. (1) and assuming a steady state, we impose geostrophic balance at $t = 0$ to find the two equations for the horizontal velocity and pressure gradients,

$$fv = \partial_x \mathcal{P};\ -fu = \partial_y \mathcal{P}.$$

Taking the partial derivative with respect to x of the first equation and adding it to the partial derivative with respect to y of the second gives the equation for the pressure,

$$\nabla_\perp^2 \mathcal{P} = f\omega_z,$$

which is translated into Fourier space as $\hat{\mathcal{P}} = -(f/k_\perp^2)\hat{\omega}_z$ (with the hats denoting the Fourier transform). In the vertical direction, there is no effect of the Coriolis force but gravity now comes in. Assuming hydrostatic momentum balance in the vertical then yields

$$\vartheta = -\frac{1}{N}\partial_z \mathcal{P},$$

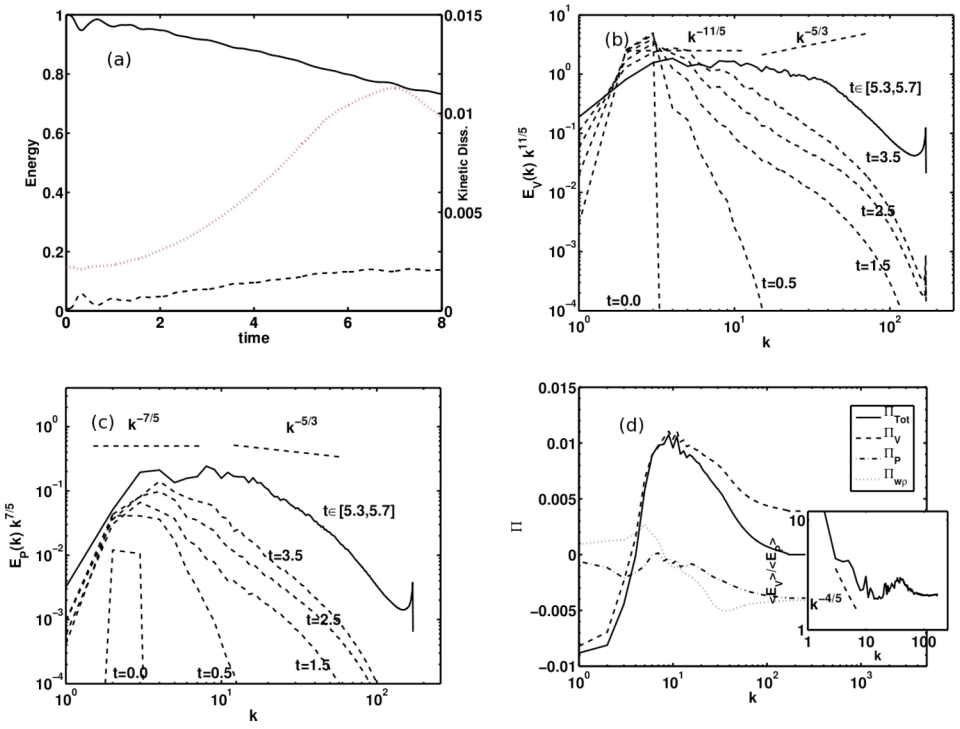

FIG. 4. Data for run B on a grid of 512^3 points with balanced initial conditions (see Sec. IV B). (a) Temporal evolution of kinetic and potential energies (solid and dashed lines) and of total dissipation (dotted line, see also Fig. 1). (b) Time evolution of kinetic energy spectra compensated by $k^{11/5}$. The solid line is the spectrum averaged over the time interval $t \in [4.8,\ 5.2]$ corresponding to the peak in enstrophy. (c) Time evolution of potential energy spectra compensated by $k^{7/5}$. The solid line is the spectrum averaged over the same time interval. (d) Energy fluxes as in Fig. 3(d) for this new run, averaged over the same time interval. In the inset is plotted, the ratio of kinetic to potential energy spectra, each averaged again over the same time interval.

which leads in Fourier space to the initial condition we seek for the scalar fluctuations, namely, $\hat{\vartheta} = -i(k_z/N)\hat{\mathcal{P}}$.

Even though the initial conditions are different, the parameters of run B are kept similar to those of run A, except for the smaller Reynolds number because of the reduced resolution. They are specifically $N = 13.2, N/f = 4.95, \nu = \kappa = 3.2 \times 10^{-4}$. The temporal dynamics of this run leads at the peak of dissipation to $Re \approx 6600$, $Fr \approx 0.026$, $U_{rms} \approx 0.85$, $L_{int} \approx 2.5$, $\ell_z \approx 0.15$, and $R_B \approx 4.4$; the resulting vertical Froude number is again only slightly smaller than one (≈0.4).

In Fig. 4(a), we show the temporal evolution of the kinetic and potential energies and of the total dissipation; they evolve in a manner very similar to run A, but with oscillations of smaller amplitude, and with a slight progressive growth of potential energy. We note that, even though there is no potential energy initially in run A, the presence of strong gravity waves builds it fast, whereas in the initially geostrophically balanced case, that growth is more likely on the slower nonlinear timescale. The kinetic and potential energy spectra are given, respectively, in Figs. 4(b) and 4(c) together with their build-up in time due to non-linear interactions (see labels). The solid lines give the spectra averaged temporally around the peak of enstrophy ($t \in [4.8,\ 5.2]$, an interval representing the same number of gravity wave periods as in run A). Furthermore, the spectra are compensated by the respective expected spectral laws for a Bolgiano-Obukhov scaling. It appears remarkably accurate again in this case. The fit to the spectral index for the kinetic energy is ≈ -2.3 over the wavenumber range $k \in [2,\ 16]$, close to the reference slope indicating BO scaling, and the fit for the potential energy in the same range is ≈ -1.5. At this lower resolution, the small-scale Kolmogorov-like spectrum is not realized, the energy decaying faster at large wavenumbers. The fits thus give spectral indices that are slightly further from the BO prediction than for run A; this may be

due to the fact that the spectra for $k > K_{BO}$ are steeper than for run A and alter the dynamics in the BO range itself.

Finally, Fig. 4(d) gives the energy fluxes (see Fig. 3(d) for a description). The fluxes are remarkably different from run A and are a signature of the different roles the inertia-gravity waves play for both runs; in run A, unbalanced, these waves are prominent whereas in run B they are almost negligible and the (usual) advection flux is the strongest. We also note that the negative fluxes are comparable for these two runs, but the flux of total energy to small scales is half what it was in run A and the turbulence is thus weaker in that case, not so much we conjecture because of the lesser Reynolds number but rather because the initially balanced flow is effective in weakening the nonlinear interactions.

We thus conclude from the examination of these figures that the BO scaling also applies in this case. Finally, we note that, while there is a somewhat discernible change in the kinetic and potential energy spectra at around $k \geq 10$, we cannot use the BO phenomenology in Eq. (17) to verify where this break should be because there is no transition to a Kolmogorov-like spectrum following the BO scaling. However, the ratio $E_V(k)/E_P(k)$ (inset of Fig. 4(d)) behaves in the same way as in run A, with a rapid decay at large scale compatible with $k^{-4/5}$ scaling, and a near equilibrium achieved at $k \approx k_c$ as in run A; furthermore, it displays a similar value for k_c which we can conclude is thus determined by the overall dimensionless parameters of the run. Similar results for the other variables are obtained for this run; for example, the helicity remains small in relative terms, and with a rather flat spectrum.

C. The lack of isotropy

The transition in the spectral slope at $k_c \approx 12$ is not visible in the total energy flux; this was already noticed in Ref. 31 in the purely rotating case: even though characteristic time scales and nonlinear dynamics change with wavenumber, the flow of energy across scales is smooth. However, the wavenumber k_c marks a clear transition in the character of the spectra, exhibiting also a sharp decrease of the ratio of kinetic to potential energy at large scales (see Fig. 3(d)), followed by a quasi-equipartition between both energies for $k \geq k_c$ all the way to the dissipative scale (although with a slight variation with wavenumber). This change of behavior in the ratio of kinetic to potential energy at $k \approx k_c$ clearly indicates that wavenumbers $k \geq k_c$ corresponds to scales dominated by energetic exchanges between nonlinear eddies and wave modes eventually leading to the quasi-equipartition between kinetic and potential energies expected for strongly stratified flow,[8] while wavenumbers $k < k_c$ are sensitive to the effect of both buoyancy and rotation. Finally, at the smallest scales of the flow dominated by dissipation processes, there is a broad decrease of kinetic energy compared to potential energy which is likely a manifestation of overturning resolved in the small scales and leading to dissipative events and mixing (see also Fig. 10 below).

Moreover, in the presence of rotation and stratification, the flow loses its mirror symmetry. A measure of the departure from mirror symmetry can be obtained from the examination of the relative helicity spectrum, defined here in absolute value terms as

$$\sigma_V(k) = |H_V(k)|/[kE_V(k)], \tag{19}$$

with $\sigma_V(k) \leq 1\ \forall k$ through a Schwarz inequality; $\sigma_V(k)$ is shown in Fig. 5(a). In HIT, $E(k) \sim k^{-e}$ and $H(k) \sim k^{-h}$ with $e = h = 5/3$ so that $\sigma_V(k) \sim 1/k$ indicating a (slow) return to mirror symmetry in the small scales. In our case, the evolution is different: $\sigma_V(k)$ is rather flat for small wavenumbers and decays as $\sim k^{-3/2}$ for wavenumbers larger than k_c. In the purely rotating case, it can be shown using dimensional arguments[59] that $e + h = 4$, on the basis of a small-scale flux dominated by helicity which is an ideal invariant in that case (though not here). Assuming that the large-scale flow is dominated by rotation in a quasi-geostrophic regime, this leads to $e \approx 5/2$, close (but not identical) to the value found here for $k < k_c$, namely, $e \approx 11/5$. It should be noted that this regime with $e = 5/2$ corresponds to a fully helical flow ($\sigma_V(k) = 1\ \forall k$), a state which is known to be unstable,[60] and therefore an energy spectrum slightly shallower than $k^{-5/2}$ should be expected instead. This energy spectrum (together with the flat spectrum of helicity) ends at a wavenumber $\approx k_c$, and one enters a rapid decrease of the helicity with wavenumber, slightly steeper than $1/k$, and

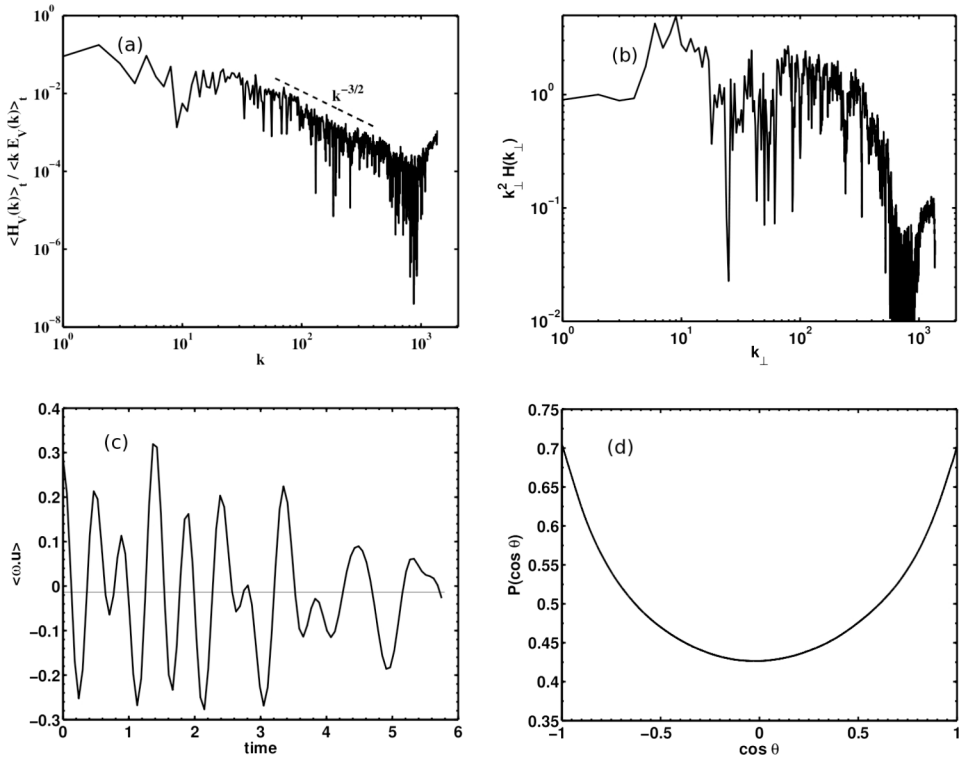

FIG. 5. Helicity dynamics using the data from the 4096^3 run A. (a) Relative helicity spectrum $|H_V(k)|/[kE_V(k)]$, which is seen as rather flat at large scale and decaying faster than $1/k$ at small scale. (b) Perpendicular spectrum of the helicity compensated with $k_\perp^2$. Note the region of excess helicity for small wavenumbers followed, for $k > k_c$ with $k_c \approx 12$, by a drop in the amplitude of the compensated spectrum, and with fluctuations associated with rapid changes in sign of the helicity. For $k > 300$, a sharp overall drop is observed. (c) Temporal evolution of the volume integrated helicity. (d) Probability distribution function of the relative helicity (cosine of the angle between velocity and vorticity) averaged about the peak of dissipation. Alignment and anti-alignment of $\mathbf{u}$ and ω are equally likely, as in homogeneous isotopic turbulence.

with strong fluctuations likely corresponding to frequent changes of sign in the helicity at various scales.

In Fig. 5(b) is presented the helicity spectrum $H(k_\perp)$ compensated with $k_\perp^2$. Note the region of excess helicity for small wavenumbers followed, for $k > k_c$ with $k_c \approx 12$, by a drop in the amplitude of the compensated spectrum, and with fluctuations associated with rapid changes in sign of the helicity. For $k > 300$, a sharp drop is observed. Indeed, for wave numbers $k \lesssim k_c$, the compensated spectrum concentrates most of the helicity, which then decreases abruptly. This excess helicity at intermediate scales may derive from the alignment of the vortical structures produced by the rotation with vertical motions caused by buoyancy due to strong stratification and may represent the physical mechanism for the generation of helicity proposed in Refs. 61 and 62 and seen in direct numerical simulations in Ref. 17. In Fig. 5(c), we also show the temporal behavior of the volume-averaged helicity. The flow starts with some residual positive helicity (resulting from the random initial conditions), but after $t \lesssim 4$ helicity fluctuates around a value close to zero. The lack of preference towards anti-alignment or alignment of velocity and vorticity can also be seen in Fig. 5(d), which displays an average of PDFs of the cosine of the angle between velocity and vorticity. Note that instantaneous PDFs (not shown) can display some slight excess at ± 1, corresponding to the fluctuations in the global helicity given in Fig. 5(c).

In the presence of rotation and stratification, the flow also loses its isotropy. In Fig. 6(a), we show for run A the ratio of $E_{3D}(k_\perp)/e(k_\perp, k_\parallel = 0)$, as defined in Eqs. (6) and (9). Both the numerator and denominator are averaged about the peak of dissipation on the time interval $t \in [5.3, 5.7]$. This plot shows that at very large scales, there is a roughly constant and small amount of energy in the 3D modes compared with that in the 2D modes. Rotation seems to play a role at these scales, mediating

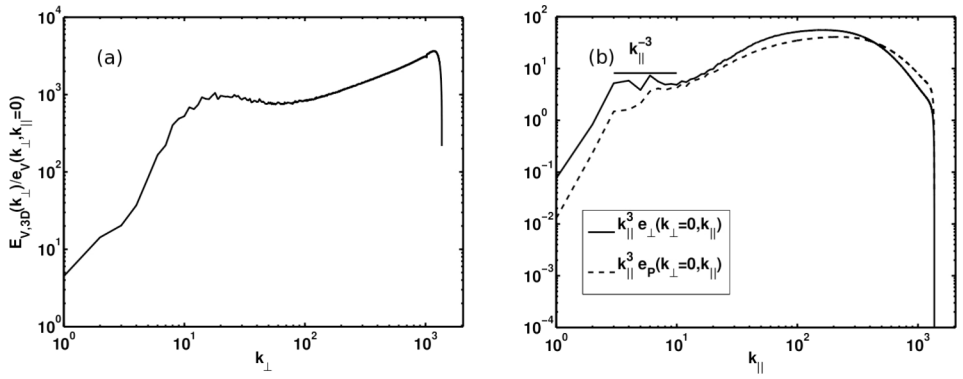

FIG. 6. (a) Ratio $E_{3D}(k_\perp)/e(k_\perp, k_\parallel = 0)$ of spectral energy in 3D modes *versus* that in 2D modes for perpendicular wave numbers. Note again the transitions for $k \approx 12$, together with one at $k \approx 120$. (b) Parallel spectrum of horizontal kinetic energy $e_\perp(k_\perp = 0, k_\parallel)$ (solid line, see Equation (7)) and parallel spectrum of potential energy $e_P(k_\perp = 0, k_\parallel)$ (dashed line), both compensated by $k_\parallel^{-3}$. All spectra are averaged over the peak of enstrophy, $t \in [5.3,\ 5.7]$ and refer to run A. Note the small flat range at large scales in $e_\perp$, both ending with equipartition at $k \approx 12$ for a small range of scales.

the distribution of kinetic energy between 2D and 3D modes and accumulating more energy in 2D modes.[21] As larger $k_\perp$ wavenumbers are considered, this distribution changes rapidly until it reaches a local maximum around k_B. After a small decrease, the amount of energy in 3D modes far outpaces the distribution among 2D modes as expected in strongly stratified flows, as energy is transferred to large $k_\perp$ and potential modes are excited. In other words, the ratio $E_{3D}(k_\perp)/e(k_\perp, k_\parallel = 0)$ is consistent with a scenario in which the rotation, effective at large scales (presumably for $k < k_\Omega$), controls the anisotropy, while at smaller scales as the system becomes dominated by stratification at the buoyancy scale, $k_B \approx 16$, the energy is transferred towards modes with small $k_\perp$ but with $k_\parallel \neq 0$, resulting in most of the energy being in 3D modes.

According to Ref. 8, under conditions of strong stratification ($Fr \to 0$), the equations describing the flow become self-similar. With rotation, self-similarity still holds, and it is suggested in Ref. 8 that the buoyancy scale defined in Eq. (13) now takes the modified form

$$\tilde{L}_B = U_0 \mathcal{F}(Ro)/N = L_B \mathcal{F}(Ro), \tag{20}$$

with $\mathcal{F}(Ro) \to 1$ when $Ro \to \infty$ and $\mathcal{F}(Ro) \to Ro^{-1}$ when $Ro \to 0$. In this latter limit, the rotating-buoyancy scale becomes $\tilde{L}_B = L_0[f/N]$. As such, note that it involves now the horizontal and vertical directions associated with stratification and rotation; it can be interpreted as well as having the dynamics organizing itself energetically so that structures are slanted in a ratio N/f. In other words, under the effect of increasing rotation at fixed stratification, the scale at which the effective Froude number in the vertical is of order unity increases as well, meaning that the large scales are more unstable. In the quasi-geostrophic (QG) limit, for strong rotation and strong stratification, one can write that $NL_v/f = L_\perp$, a relationship that can be obtained simply, for example, by equating in the dispersion relation the terms due to rotation and to stratification. This therefore can define an aspect ratio of structures for which rotation and stratification balance each other. Writing that $L_\perp$ is the integral scale $L_{int} \approx 2.6$, we now find for the wavenumber where a change of behavior occurs between a rotation-dominated regime to a stratification dominated regime to be $\tilde{k}_B \approx 12$, a value that is in good agreement with k_c as a break-point identified on several of the spectra presented here. To reconcile this with the evaluation of K_{BO} given earlier, we could conjecture that the energetics of the flow at large scale is dominated by the buoyancy but the precise scale distribution of the energy is governed by the rotation as in the QG limit.

In Fig. 6(b), we also show plots of $e_\perp(k_\perp = 0, k_\parallel)$ and of the spectrum of potential energy, both compensated by $k_\parallel^{-3}$ and shown at the peak of enstrophy. It has been predicted[8] that $e_\perp(k_\perp = 0, k_\parallel) \propto k_\parallel^{-3}$, and similarly that the spectrum of the temperature fluctuations should also scale as $e_P \propto k_\parallel^{-3}$. The figure shows the existence of this prediction in the kinetic energy, but if such a range exists in the potential energy, it is rather narrow. Both spectra seem to develop shallower power

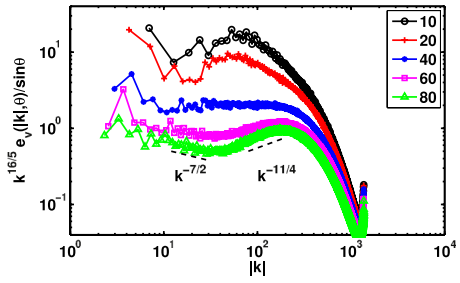

FIG. 7. Angular kinetic energy spectra $e(|k|,\theta)$ defined in (Eq. (6)) for various co-latitudes, θ, (in deg) averaged over the peak of enstrophy, $t \in [5.3,\ 5.7]$ in run A and compensated by $k(\theta)^{-16/5}$: $\theta = 10°$ (black circles), $\theta = 20°$ (red crosses), $\theta = 40°$ (blue asterisk), $\theta = 60°$ (magenta squares), and finally $\theta = 80°$ (green triangles). The compensating slope corresponds to an (uncompensated) isotropic (BO) scaling of $k^{-11/5}$.

laws for $k > k_c$. For $k > k_B$, the temperature and horizontal kinetic energy in these spectra are in approximate equipartition, which is expected for a self-similar range corresponding, in the primitive equations, to a balance between nonlinearity and wave dynamics. Note that a $k_\parallel^{-3}$ spectrum is often observed in the ocean and is called the saturation spectrum; it is the regime in which, at least in the purely stratified case, intermittency of the vertical velocity has been found.[63]

Finally, in Fig. 7 are shown the angular spectra for the kinetic energy, (cf. Eq. (6)) for several values of the co-latitude, θ, i.e., the angle between the wave-vector **k** and the vertical. All spectra are averaged evenly around the peak of dissipation using ten temporal snapshots and are compensated by $k_\perp^{-16/5}$, which is equivalent to compensating the isotropic spectra by $k^{-11/5}$ (see the discussion after Eq. (6)). The angular spectra are computed by interpolating the time-averaged 2D axisymmetric spectra along the line at a given co-latitude using a cubic interpolating polynomial. All scales are anisotropic, except close to the dissipative range; this is expected, since, in this simulation, $k_{OZ} \approx 431$ and $k_\eta \approx 660$ (see Sec. II D). Due to the dispersion relation, Eq. (5), as $\theta \to 0$, inertial waves will dominate gravity waves, and as $\theta \to \pi/2$, the reverse will occur; the angular spectra reflect roughly a continuum in this behavior. The apparent tendency at small co-latitude for the spectrum to become very steep at large scales suggests a quasi-two-dimensionalisation due to strong rotational effects.[14] At $\theta = 20$, the steep range governed by strong rotation at the largest scales gives way to a BO scaling at around $k \sim 10$ for a short range, and the BO scaling range seems to spread to larger scales as θ approaches intermediate values. But as the perpendicular direction is reached, multiple spectral ranges emerge after the BO scaling ends at the break-point $k = k_c \sim 12$. In fact, a new characteristic scale seems to materialize at $k \sim 45$ for the largest co-latitudes that may serve to separate distinct dynamical balances as illustrated by the reference slopes.

V. STRUCTURES

The salient physical structures that develop in this flow are relatively large, slanted layers, as can be seen in Fig. 8 displaying the horizontal and vertical velocities. The plots are perspective volume renderings of a thin y-z slab. The variation in the vertical direction is seen in these plots to be large, varying from filamentary-like thickness to structures at the integral scale, which are comparable to the domain size. The velocity is dominated by its perpendicular component, as already noted in Fig. 2(a).

As expected, the vorticity displays more small-scale variation. Figure 9(a) shows the vertical vorticity at the peak of enstrophy in a horizontal plane for the full box and at one-half, the linear resolution of the computation; contrary to Fig. 8, this is an actual slice (i.e., it is not a volume rendering), and thus, it has no depth. We have $\omega_{rms} \approx 17.5$ and $\omega_{max} \approx 840$, to be contrasted with $f = 2.66$, indicative of the presence of locally strong vortices dominating the imposed rotation. Globally, the flow is seen to be composed of large-scale vortices at roughly the size of the initial conditions and separated by thick slanted vortex lanes with a complex tangle of small-scale intense vortices. A zoom at full 4096^2 resolution (Fig. 9(b)) indicates that small-scale features are

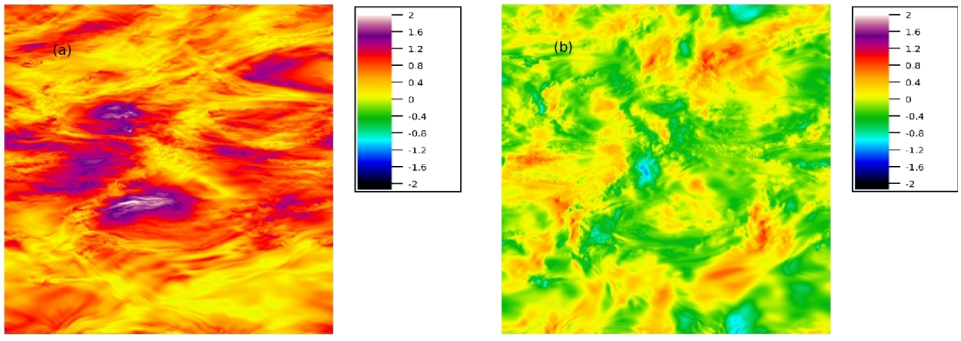

FIG. 8. Perspective volume renderings of a thin sub-volume in x, with full size in the y-z plane, at $t = 5.54$ (close to the peak of enstrophy); the slab thickness in the x (depth) direction is 0.04 times the box size. All renderings were made using the VAPOR visualization system.[56] The y-axis is directed horizontally and the z-axis, vertically. Presented are (a) perpendicular and (b) vertical velocity with identical color mapping. Note that the perpendicular velocity is dominant in magnitude (see also Fig. 2(a)). This and subsequent visualizations are from run A.

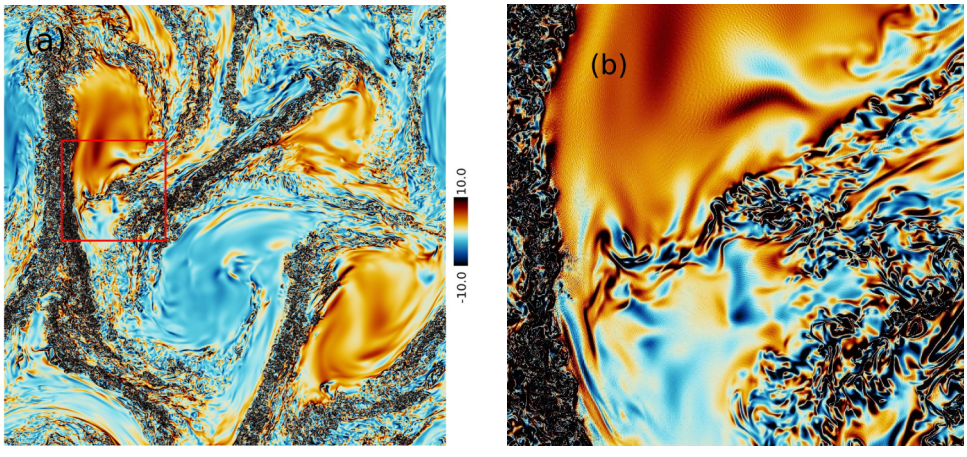

FIG. 9. (a) Color image of the vertical component of the vorticity at $t = 5.54$ (close to the peak of enstrophy) for the full box in a horizontal plane located at 0.45 times the vertical box length. The x-axis is directed horizontally and the y-axis, vertically. A resolution of 2048×2048 is shown, reduced from the full original resolution of 4096×4096. The red box indicates the area zoomed in upon in (b) at full resolution. Note that $\omega_{rms} \approx 17.5$ and $\omega_{max} \approx 840$ (to be compared with $f = 2.66$). Note also the simultaneous presence of large vortices and elongated vortex lanes made up of intense local vortices which once zoomed upon (as in (b)) display an intricate and convoluted network of small-scale structures (see also Fig. 10 for a zoom on structures for a vertical cut).

well-resolved in this run and are composed of a convoluted network of vortices, originating from many local instabilities that develop in this flow. The large-scale vortices seen in this slice are observed at most other flow planes, but it is unclear if they represent cross sections of coherent columns such as the Taylor-like columns seen in pure rotating flows. They are, however, related to the role played by rotation, as already noted when examining the energy flux. In previous studies, the aspect ratio of the vortices has been found to depend on the global value of N/f through, for example, the variation of correlation length scales.[9,66] It also depends on local values, as determined, for example, by the local rotation of the vortex.[67]

Additionally, in Fig. 10 are presented several renderings of a thin x-z slab, zooming in on an area of 0.12×0.1 times the box size, comparable to the vertical Taylor scale. Note that ℓ_{OZ} is about 1/3 of this slab size. These visualizations show scales at which overturning can occur and demonstrate the clear onset of Kelvin-Helmholtz instabilities due to shear layers. In both Figs. 8 and 10, the thickness of the layers being visualized is 0.01 in terms of the box size, roughly one Kolmogorov (dissipation) length.

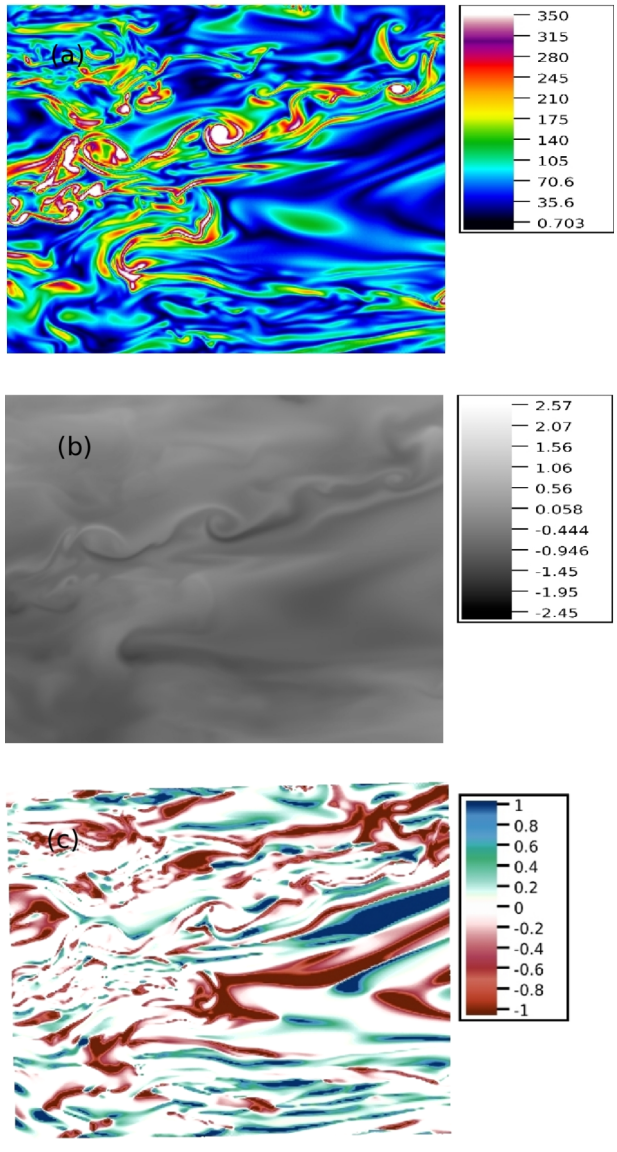

FIG. 10. Perspective volume renderings of a thin x-z sub-volume of size 0.12×0.1 times the compute box size at $t = 5.54$ (close to the peak of dissipation); the slab thickness in the y-direction is 0.01 times the box size. The x-axis is directed horizontally, and the z-axis, vertically. Presented are (a) vorticity magnitude, (b) temperature fluctuations, and (c) local Richardson number Ri_g defined in Equation (14). The color bar of vorticity illustrates the relatively intense vortices that are generated, and note the slanted Kelvin-Helmholtz layer.

We note that, in the simplified geometry used in this paper, one does not observe structures such as mushrooms and rolls which are usually associated with comparably idealized systems but with top and bottom thermal boundaries, and which can be either fully convective or stably stratified. The convective rolls can form at moderate Rayleigh number and are created and sustained by small scale plumes that detach from the boundary layer; flows characterized by transient turbulent plumes occur at still higher Rayleigh number (see, e.g., Ref. 68 for experimental observations). The striking contrast between the quiescent large-scale vortices and the intense vortex lanes with strong gradients that separate them is rather reminiscent of the structures that develop in turbulent flows through a positive feedback mechanism between waves and turbulent mixing as invoked in Refs. 69 and 70.

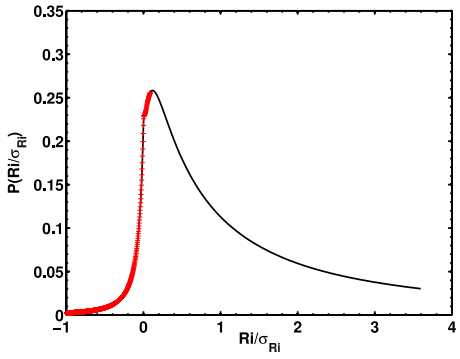

FIG. 11. Probability distribution function of the gradient Richardson number defined in Eq. (14), at the latest time in the run A simulation. The (red) crosses indicate where $Ri_g \leq 0.25$, the classical criterion for overturning instability.[64,65]

In Fig. 10, a clear vortex street appears at that time in the vorticity (Fig. 10(a)), the density (Fig. 10(b)) and the gradient Richardson number (Fig. 10(c)) defined in Eq. (14), showing that the flow can be locally unstable to overturning. Note the strong correlation between vorticity and temperature fluctuations and the fact that the most unstable regions of the flow at this time are not strongly linked to the vortex street but that, in fact, other layers are being destabilized. Note also the inter-mingling of stable and unstable structures at these scales. As mentioned earlier, the Richardson number based on velocity gradients (which can be defined in terms of ℓ_z) can be considered as an overall index of the potential instability of the flow. A decrease in ℓ_z can thus be interpreted as leading to a more negative gradient Richardson number, which is indicative of an evolution towards a flow more prone to overturning instability. Indeed, the probability distribution function of Ri_g shown in Fig. 11 indicates a strong probability of the flow meeting the classical criterion for overturning. It was found in Ref. 39 that Ri can become negative above $R_\lambda \approx 900$, with the change in sign coming from the change in sign of the vertical gradient of density. These results indicate that instabilities are triggered at various locations in the flow. In fact, actual bumps in the energy spectra have been observed in Ref. 39 at times of minima in the Richardson number for sufficiently high R_λ that correspond to Kelvin-Helmholtz instabilities feeding directly the small scales.

VI. CONCLUSION

We have analyzed in this paper the results obtained from a high Reynolds number run of rotating stratified turbulence with $N/f = 4.95$, characteristic of the abyssal southern ocean at mid latitudes. With a Froude number of ≈ 0.024 and $Re \approx 5.5 \times 10^4$, this run is not realistic in terms of Reynolds number for geophysical fluid dynamics, and we have chosen to emphasize an examination of scales that are still dominated by the waves, with a barely resolved isotropic Kolmogorov range at small scales. To unravel the role played by different phenomena, we examine the partition of several fields among scales. We conclude that the largest scales (for $k < k_0$) are dominated by rotation, with a negative energy flux, and that for scales larger than a critical scale, or for $k_0 < k < k_c$, the constant-flux range is one where the source of the energy is the potential energy stored in the large-scale gravity waves. We have presented evidence that this energy source leads potentially to a Bolgiano-Obukhov scaling (Eq. (16)). We have also demonstrated that this scaling is not necessarily inconsistent with the self–similarity argument of Ref. 8, and we have shown that it is also obtained for initial conditions which are in geostrophic balance.

The steep power-law observed at large scale is consistent with many oceanic observations, as analyzed, for example, in Refs. 24 and 71. The tendency for energy to pile-up in the large scales, even in the spin-down case, was already noted in Ref. 72, where the inverse transfer was attributed to the geostrophic modes, whereas the wave modes undergo a direct energy cascade (for a high-resolution forced case using hyper-viscosity, see Ref. 73). At smaller scales, a Kolmogorov spectrum, in terms of horizontal wave numbers, obtains before isotropy is recovered, as already

found in several studies of stratified flows. In addition to the conspicuous Kelvin-Helmholtz instabilities observed at small scale, strong mixing at small scale is clearly favored as indicated both by an overall Froude number based on a vertical length scale of order unity and by a PDF of the gradient Richardson number that shows directly the significant likelihood of overturning instability.

The extent in wavenumber of the Bolgiano-Obuknov scaling range is determined by the fact that K_{BO} defined in Eq. (17) must be larger than the wavenumber corresponding to the scale at which the initial conditions are set. This has been discussed thoroughly in the literature, for example, in the context of convectively unstable flows (see, e.g., Refs. 46 and 49 and references therein). In the purely stratified case, it is shown in Ref. 51 that simply increasing the Richardson number increases K_{BO}. But this computation uses a forcing that imposes bi-dimensionalization directly, so a flow that does not use such a forcing may easily develop in such a way as to counteract this effect. In RST, rotation is bound to play a role as well and direct some of the energy towards large scales in the forced case. But in both cases, a strong stratification is a prerequisite, as well as a high Reynolds number so that R_B be sufficiently large that a Kolmogorov range develop at small scale. For atmospheric observations, the same ideas likely hold: an extended BO scaling is likely in regions of large Ri where $\mathcal{R}_B$ is sufficiently large as well. It has been conjectured[46] that in addition to strong stratification, the Bolgiano-Obukhov scale shows a variation with Prandtl number, Pr, as $K_{BO} \sim Pr^{1/4}$. Then, the Kolmogorov dissipation scale relates to K_{BO} via $k_\eta/K_{BO} \sim Pr^{-1/2}$, suggesting that the larger the Pr becomes, the more difficult it becomes to isolate the physics of the convective Bolgiano-Obukhov scaling from dissipative effects without scale separation that is very high for both the kinetic and potential energies, and this is one of the chief challenges in verifying this Pr dependence numerically using DNS.

The regime with small Froude number and yet large buoyancy Reynolds number and moderate rotation, characteristic of many flows in geophysical fluid dynamics, remains a computational challenge, in particular when assessing highly non-local interactions between large scales fed by the inverse cascade of energy in the presence of rotation, even if weak, and small scales fed by the direct cascade of energy. Non-local interactions have been identified in such flows, for example, in purely rotating flows,[74] in the context of the zig-zag instability,[75] and in rotating stratified turbulence.[28] This clearly points out the need to resolve the large-scale as well as the small-scale dynamics. In this regard, fundamental and idealized studies such as the one presented in this paper will remain valuable for some time to come, if only because they may lead to improved anisotropic and multi-scale parametrisations of such flows.

Many issues remain unexplored and one should analyze in detail, for example, the distribution of energy among the normal modes of the flow (see, e.g., Refs. 20, 27, and 66), the small-scale behavior of the flow, and the role that helical coherent structures can play in mixing, transport, and intermittency in RST flows, as, for example, in tropical cyclogenesis.[76] Indeed, helicity or velocity-vorticity correlations are an ideal ($\nu = 0$) invariant of the homogeneous isotropic case (as well as in the presence of solid body rotation), but when stratification is added, it can be created—as evidenced here—by quasi-geostrophic large-scale flows as a consequence of thermal winds.[17,62] It is known that, for HIT in the presence of helical coherent structures, mixing is modified. There are already sub-grid scale models of turbulence showing that, when taking helicity into account, the modeling capability is enhanced in a measurable fashion,[77,78] and thus, the present study at high resolution may provide a useful database for testing a variety of parametrization schemes.

ACKNOWLEDGMENTS

This work was supported by CMG/NSF Grant No. 1025183 and used resources of the Oak Ridge Leadership Computing Facility (OLCF) at the Oak Ridge National Laboratory, which is supported by the Office of Science of the U.S. Department of Energy under Contract No. DE-AC05-00OR22725. Computer time was provided through a DOE INCITE Award No. ENP008 and an NSF XSEDE allocation Award No. TG-PHY110044. We wish to thank M. Matheson of the OLCF for his full-res visualizations. Additional computer time through an ASD allocation at NCAR is also gratefully acknowledged. P.D.M. is a member of the Carrera del Investigador Científico of CONICET. Support for A.P., from LASP and Bob Ergun, is gratefully acknowledged. R.M.

acknowledges support from the Regional Operative Program Calabria ESF 2007/2013, and Marie Curie Project FP7PIRSES-2010-269297-Turbo-plasmas.

This manuscript has been authored by UT-Battelle, LLC under Contract No. DE-AC05-00OR22725 with the U.S. Department of Energy. The United States Government retains and the publisher, by accepting the article for publication, acknowledges that the United States Government retains a non-exclusive, paid-up, irrevocable, world-wide license to publish or reproduce the published form of this manuscript, or allow others to do so, for United States Government purposes. The Department of Energy will provide public access to these results of federally sponsored research in accordance with the DOE Public Access Plan (http://energy.gov/downloads/doe-public-access-plan).

[1] Y. Kaneda, T. Ishihara, M. Yokokawa, K. Itakura, and A. Uno, "Energy dissipation rate and energy spectrum in high-resolution DNS of turbulence in a periodic box," Phys. Fluids **15**, L21–L24 (2003).
[2] T. Ishihara, T. Gotoh, and Y. Kaneda, "Study of high Reynolds number isotropic turbulence by direct numerical simulation," Ann. Rev. Fluid Mech. **41**, 165–180 (2009).
[3] B. Sawford and P. K. Yeung, "Kolmogorov similarity scaling for one-particle Lagrangian statistics," Phys. Fluids **23**, 091704 (2011).
[4] B. Sawford and P. K. Yeung, "Turbulent Lagrangian velocity statistics conditioned on extreme values of dissipation," Proceedings, IUTAM **9**, 129–137 (2013).
[5] S. Almalkie and S. de Bruyn Kops, "Kinetic energy dynamics in forced, homogeneous, and axisymmetric stably stratified turbulence," J. Turbul. **13**, 29 (2012).
[6] C. Cambon and L. Jacquin, "Spectral approach to non-isotropic turbulence subjected to rotation," J. Fluid Mech. **202**, 295–317 (1989).
[7] R. Marino, P. D. Mininni, D. Rosenberg, and A. Pouquet, "Anisotropy and inverse cascades in stratified turbulence: Gravity waves and transient transfer," Phys. Rev. E **90**, 023018 (2014).
[8] P. Billant and J.-M. Chomaz, "Self-similarity of strongly stratified inviscid flows," Phys. Fluids **13**, 1645–1651 (2001).
[9] E. Lindborg, "The effect of rotation on the mesoscale energy cascade in the free atmosphere," Geophys. Res. Lett. **32**, 1–4, doi:10.1029/2004GL021319 (2005).
[10] L. Liechtenstein, F. Godeferd, and C. Cambon, "Nonlinear formation of structures in rotating stratified turbulence," J. Turbul. **6**, 1–18 (2005).
[11] L. Liechtenstein, F. S. Godeferd, and C. Cambon, "Time evolution of structures in rotating and stratified turbulence," Flow, Turbul. Combust. **76**, 419–427 (2006).
[12] M. Waite and P. Bartello, "The transition from geostrophic to stratified turbulence," J. Fluid Mech. **568**, 89–108 (2006).
[13] H. Hanazaki, "Linear processes in stably and unstably stratified rotating turbulence," J. Fluid Mech. **465**, 157–190 (2002).
[14] L. Smith and F. Waleffe, "Generation of slow large scales in forced rotating stratified turbulence," J. Fluid Mech. **451**, 145–168 (2002).
[15] S. Kurien and L. M. Smith, "Asymptotics of unit burger number rotating and stratified flows for small aspect ration," Physica D **241**, 149–163 (2012).
[16] M. Remmel, J. Sukhatme, and L. Smith, "Nonlinear inertia-gravity wave-mode interactions in three dimensional rotating stratified flows," Commun. Math. Sci. **8**, 357–376 (2010).
[17] R. Marino, P. D. Mininni, D. Rosenberg, and A. Pouquet, "Spontaneous emergence of helicity in rotating stratified turbulence," Phys. Rev. E **87**, 033016 (2013).
[18] J. Molinari and D. Vollaro, "Distribution of helicity, CAPE, and shear in tropical cyclones," J. Atmos. Sci. **67**, 274–284 (2010).
[19] M. Nikurashin, G. K. Vallis, and A. Adcroft, "Routes to energy dissipation for geostrophic flows in the Southern Ocean," Nat. Geosci. **6**, 48–51 (2012).
[20] C. Herbert, A. Pouquet, and R. Marino, "Restricted equilibrium and the energy cascade in rotating and stratified flows," J. Fluid Mech. **758**, 374–406 (2014).
[21] R. Marino, P. D. Mininni, D. Rosenberg, and A. Pouquet, "Inverse cascades in rotating stratified turbulence: Fast growth of large scales," Europhys. Lett. **102**, 44006 (2013).
[22] A. Pouquet and R. Marino, "Geophysical turbulence and the duality of the energy flow across scales," Phys. Rev. Lett. **111**, 234501 (2013).
[23] R. Marino, A. Pouquet, and D. Rosenberg, "Resolving the Paradox of Oceanic Large-Scale Balance and Small-Scale Mixing," Phys. Rev. Lett. **114**, 114504 (2015).
[24] B. Arbic, K. Polzin, R. B. Scott, J. Richman, and J. Shriver, "On eddy viscosity, energy cascades, and the horizontal resolution of gridded satellite altimeter products," J. Phys. Oceanogr. **43**, 283–300 (2013).
[25] C. R. Doering and J. D. Gibbon, *Applied Analysis of the Navier Stokes Equations* (Cambridge University, 1995).
[26] T. Warn, "Statistical mechanical equilibria of the shallow water equations," Tellus **38A**, 1–11 (1986).
[27] P. Bartello, "Geostrophic adjustment and inverse cascade in rotating stratified turbulence," J. Atmos. Sci. **52**, 4410–4428 (1995).
[28] H. Aluie and S. Kurien, "Joint downscale fluxes of energy and potential enstrophy in rotating stratified Boussinesq flows," Eur. Phys. Lett. **96**, 44006 (2011).
[29] M. Waite, "Potential enstrophy in stratified turbulence," J. Fluid Mech. **722**, R4 (2013).
[30] P. Sagaut and C. Cambon, *Homogeneous Turbulence Dynamics* (Cambridge University Press, Cambridge, 2008).
[31] P. D. Mininni, D. Rosenberg, and A. Pouquet, "Isotropization at small scale of rotating helically driven turbulence," J. Fluid Mech. **699**, 263–279 (2012).

[32] A. Sen, D. Rosenberg, A. Pouquet, and P. D. Mininni, "Anisotropy and non-universality in scaling laws of the large scale energy spectrum in rotating turbulence," Phys. Rev. E **86**, 036319 (2012).
[33] P. D. Mininni, D. Rosenberg, R. Reddy, and A. Pouquet, "A hybrid MPI-OpenMP scheme for scalable parallel pseudospectral computations for fluid turbulence," Parallel Comput. **37**, 316–326 (2011).
[34] M.-E. Brachet, M. Bustamante, G. Krstulovic, P. D. Mininni, A. Pouquet, and D. Rosenberg, "Ideal dynamics of three-dimensional MHD flows implementing the Taylor-Green symmetries," Phys. Rev. E **87**, 013110 (2013).
[35] G. Ivey, K. Winters, and J. Koseff, "Density stratification, turbulence but how much mixing?," Ann. Rev. Fluid Mech. **40**, 169–184 (2008).
[36] M. L. Waite, "Stratified turbulence at the buoyancy scale," Phys. Fluids **23**, 066602 (2011).
[37] P. Augier, J.-M. Chomaz, and P. Billant, "Spectral analysis of the transition to turbulence from a dipole in stratified fluid," J. Fluid Mech. **713**, 86–108 (2012).
[38] P. Bartello and S. Tobias, "Sensitivity of stratified turbulence to the buoyancy Reynolds number," J. Fluid Mech. **725**, 1–22 (2013).
[39] J.-P. Laval, J. C. McWilliams, and B. Dubrulle, "Forced stratified turbulence: Successive transitions with Reynolds number," Phys. Rev. E **68**, 036308 (2003).
[40] R. B. Scott, J. A. Goff, A. C. Naveira Garabato, and A. J. G. Nurser, "Global rate and spectral characteristics of internal gravity wave generation by geostrophic flow over topography," J. Geophys. Res. **116**, C09029, doi: 10.1029/2011JC007005 (2011).
[41] A. C. Naveira Garabato, K. L. Polzin, B. A. King, K. J. Heywood, and M. Visbeck, "Widespread intense turbulent mixing in the southern ocean," Science **303**, 210–213 (2004).
[42] P. Héas, E. Mémin, D. Heitz, and P. D. Mininni, "Power laws and inverse motion modelling: Application to turbulence measurements from satellite images," Tellus A **64**, 10962 (2012).
[43] S. Kurien and L. Smith, "Effect of rotation and domain aspect-ratio on layer formation in strongly stratified Boussinesq flows," J. Turbul. **15**, 241–271 (2014).
[44] M. Bolgiano, Jr., "Turbulent spectra in a stably stratified atmosphere," J. Geophys. Res. **64**, 2226–2229, doi:10.1029/JZ064i012p02226 (1959).
[45] A. M. Obukhov, "Effect of the Archimedean forces on the structure of the temperature field in a turbulent flow," Dokl. Akad. Nauk SSSR **125**, 1246–1248 (1959).
[46] D. Lohse and K.-Q. Xia, "Small-scale properties of turbulent Rayleigh–Bénard convection," Ann. Rev. Fluid Mech. **42**, 335–364 (2010).
[47] G. Boffetta and R. Ecke, "Two-dimensional turbulence," Ann. Rev. Fluid Mech. **44**, 427–451 (2012).
[48] F. Seychelles, F. Ingremeau, C. Pradere, and H. Kellay, "From intermittent to nonintermittent behavior in two dimensional thermal convection in a soap bubble," Phys. Rev. Lett. **105**, 264502 (2010).
[49] E. S. C. Ching, Y.-K. Tsang, and T. N. Fok, "Scaling behavior in turbulent Rayleigh–Bénard convection revealed by conditional structure functions," Phys. Rev. E **87**, 013005 (2013).
[50] G. Boffetta, F. de Lillo, A. Mazzino, and S. Musacchio, "Bolgiano scale in confined Rayleigh–Taylor turbulence," J. Fluid Mech. **690**, 426–440 (2012).
[51] A. Kumar, A. Chatterjee, and M. Verma, "Energy spectrum of buoyancy-driven turbulence," Phys. Rev. E **90**, 023016 (2014).
[52] S. Lovejoy, A. F. Tuck, S. J. Hovde, and D. Schertzer, "Vertical cascade structure of the atmosphere and multifractal dropsonde outages," J. Geophys. Res. **114**, D07111, doi: 10.1029/2008jd010651 (2009).
[53] G. Fitton and D. Schertzer, "Scaling of turbulence in the atmospheric surface-layer: Which anisotropy?," J. Phys.: Conf. Ser. **318**, 072008 (2011).
[54] S. J. Hovde, A. F. Tuck, S. Lovejoy, and D. Schertzer, "Vertical scaling of temperature, wind and humidity fluctuations: Dropsondes from 13 km to the surface of the Pacific Ocean," Int. J. Remote Sens. **32**, 5891–5918 (2011).
[55] L. Smith, J. Chasnov, and F. Waleffe, "Crossover from two to three dimensional turbulence," Phys. Rev. Lett. **77**, 2467–2470 (1996).
[56] J. Clyne, P. D. Mininni, A. Norton, and M. Rast, "Interactive desktop analysis of high resolution simulations: Application to turbulent plume dynamics and current sheet formation," New J. Phys. **9**, 301 (2007).
[57] Y. Kimura and J. R. Herring, "Diffusion in stably stratified turbulence," J. Fluid Mech. **328**, 253–269 (1996).
[58] Y. Kimura and J. R. Herring, "Energy spectra of stably stratified turbulence," J. Fluid Mech. **698**, 19–50 (2012).
[59] A. Pouquet and P. D. Mininni, "The interplay between helicity and rotation in turbulence: Implications for scaling laws and small-scale dynamics," Philos. Trans. R. Soc. **368**, 1635–1662 (2010).
[60] O. Podvigina and A. Pouquet, "On the nonlinear stability of the 1:1:1 ABC flow," Physica D **75**, 475–508 (1994).
[61] H. K. Moffatt and A. Tsinober, "Helicity in laminar and turbulent flow," Annu. Rev. Fluid Mech. **24**, 281–312 (1992).
[62] R. Hide, "A note on helicity," Geophys. Astrophys. Fluid Dyn. **7**, 157–161 (1976).
[63] C. Rorai, P. D. Mininni, and A. Pouquet, "Turbulence comes in bursts in stably stratified flows," Phys. Rev. E **89**, 043002 (2014).
[64] J. W. Miles, "On the stability of heterogeneous shear flows," J. Fluid Mech. **10**, 496–508 (1961).
[65] L. N. Howard, "Note on a paper of John W. Miles," J. Fluid Mech. **10**, 509–512 (1961).
[66] J. Sukhatme and L. Smith, "Vortical and wave modes in 3D rotating stratified flows: Random large-scale forcing," Geophys. Astrophys. Fluid Dyn. **102**, 437–455 (2008).
[67] O. Aubert, M. Le Bars, P. Le Gal, and P. S. Marcus, "The universal aspect ratio of vortices in rotating stratified flows: Experiments and observations," J. Fluid Mech. **706**, 34–45 (2012).
[68] R. Krishnamurti and L. N. Howard, "Large-scale flow generation in turbulent convection," Proc. Natl. Acad. Sci. U. S. A. **78**, 1981–1985 (1981).
[69] D. G. Dritschel and M. E. McIntyre, "Multiple jets as PV staircases: The Phillips effect and the resilience of eddy-transport barriers," J. Atmos. Sci. **65**, 855–874 (2008).
[70] W. J. McKiver and D. G. Dritschel, "Balance in non-hydrostatic rotating stratified turbulence," J. Fluid Mech. **596**, 201–219 (2008).

[71] R. B. Scott and F. Wang, "Direct evidence of an oceanic inverse kinetic energy cascade from satellite altimetry," J. Phys. Oceanogr. **35**, 1650–1666 (2005).
[72] O. Métais, P. Bartello, E. Garnier, J. Riley, and M. Lesieur, "Inverse cascade in stably stratified rotating turbulence," Dyn. Atmos. Oceans **23**, 193–203 (1996).
[73] Y. Kitamura and Y. Matsuda, "The k_h^{-3} and $k_h^{-5/3}$ energy spectra in stratified turbulence," Geophys. Res. Lett. **33**, L05809, doi:10.1029/2005GL024996 (2006).
[74] P. D. Mininni, A. Alexakis, and A. Pouquet, "Scale interactions and scaling laws in rotating flows at moderate Rossby numbers and large Reynolds numbers," Phys. Fluids **21**, 015108 (2009).
[75] A. Deloncle, P. Billant, and J.-M. Chomaz, "Nonlinear evolution of the zigzag instability in stratified fluids: A shortcut on the route to dissipation," J. Fluid Mech. **599**, 229–239 (2008).
[76] G. Levina and M. Montgomery, "Numerical diagnosis of tropical cyclogenesis based on a hypothesis of helical self-organization of moist convective atmospheric turbulence," Dokl. Earth Sci. **458**, 1143–1148 (2014).
[77] N. Yokoi and A. Yoshizawa, "Statistical analysis of the effects of helicity in inhomogeneous turbulence," Phys. Fluids **A5**, 464–477 (1993).
[78] J. Baerenzung, P. D. Mininni, A. Pouquet, and D. Rosenberg, "Spectral modeling of turbulent flows and the role of helicity in the presence of rotation," J. Atmos. Sci. **68**, 2757–2770 (2011).